

$\Lambda_b \rightarrow p \ell^- \bar{\nu}_\ell$ and $\Lambda_b \rightarrow \Lambda_c \ell^- \bar{\nu}_\ell$ form factors from lattice QCD with relativistic heavy quarks

William Detmold,¹ Christoph Lehner,² and Stefan Meinel^{3,4,*}

¹*Center for Theoretical Physics, Massachusetts Institute of Technology, Cambridge, MA 02139, USA*

²*Physics Department, Brookhaven National Laboratory, Upton, NY 11973, USA*

³*Department of Physics, University of Arizona, Tucson, AZ 85721, USA*

⁴*RIKEN BNL Research Center, Brookhaven National Laboratory, Upton, NY 11973, USA*

Measurements of the $\Lambda_b \rightarrow p \ell^- \bar{\nu}_\ell$ and $\Lambda_b \rightarrow \Lambda_c \ell^- \bar{\nu}_\ell$ decay rates can be used to determine the magnitudes of the CKM matrix elements V_{ub} and V_{cb} , provided that the relevant hadronic form factors are known. Here we present a precise calculation of these form factors using lattice QCD with 2+1 flavors of dynamical domain-wall fermions. The b and c quarks are implemented with relativistic heavy-quark actions, allowing us to work directly at the physical heavy-quark masses. The lattice computation is performed for six different pion masses and two different lattice spacings, using gauge-field configurations generated by the RBC and UKQCD collaborations. The $b \rightarrow u$ and $b \rightarrow c$ currents are renormalized with a mostly nonperturbative method. We extrapolate the form factor results to the physical pion mass and the continuum limit, parametrizing the q^2 -dependence using z -expansions. The form factors are presented in such a way as to enable the correlated propagation of both statistical and systematic uncertainties into derived quantities such as differential decay rates and asymmetries. Using these form factors, we present predictions for the $\Lambda_b \rightarrow p \ell^- \bar{\nu}_\ell$ and $\Lambda_b \rightarrow \Lambda_c \ell^- \bar{\nu}_\ell$ differential and integrated decay rates. Combined with experimental data, our results enable determinations of $|V_{ub}|$, $|V_{cb}|$, and $|V_{ub}/V_{cb}|$ with theory uncertainties of 4.4%, 2.2%, and 4.9%, respectively.

I. INTRODUCTION

To date, all direct determinations of the CKM matrix element magnitudes $|V_{ub}|$ and $|V_{cb}|$ were performed using measurements of B meson semileptonic or leptonic decays at e^+e^- colliders. For both $|V_{ub}|$ and $|V_{cb}|$, there are tensions between the most precise extractions from exclusive and inclusive semileptonic B decays. The 2014 Review of Particle Physics lists [1]

$$\begin{aligned} |V_{ub}|_{\text{excl.}} &= (3.28 \pm 0.29) \times 10^{-3}, & |V_{cb}|_{\text{excl.}} &= (39.5 \pm 0.8) \times 10^{-3}, \\ |V_{ub}|_{\text{incl.}} &= (4.41 \pm 0.15^{+0.15}_{-0.17}) \times 10^{-3}, & |V_{cb}|_{\text{incl.}} &= (42.2 \pm 0.7) \times 10^{-3}. \end{aligned} \quad (1)$$

The exclusive results in Eq. (1) are from the decays $B \rightarrow \pi \ell \bar{\nu}$ and $B \rightarrow D^* \ell \bar{\nu}$ (where $\ell = e, \mu$) and use hadronic form factors from lattice QCD [2, 3]. The discrepancy between the exclusive and inclusive results is a long-standing puzzle in flavor physics [4–6], and right-handed currents beyond the Standard Model have been considered as a possible explanation [7–10]. New lattice QCD calculations of the $B \rightarrow \pi$ form factors published recently yield somewhat higher values of $|V_{ub}|_{\text{excl.}} = (3.72 \pm 0.16) \times 10^{-3}$ [11] and $|V_{ub}|_{\text{excl.}} = (3.61 \pm 0.32) \times 10^{-3}$ [12], but the latest analysis of $B \rightarrow D^* \ell \bar{\nu}$ using lattice QCD gives $|V_{cb}|_{\text{excl.}} = (39.04 \pm 0.75)$ [13] and slightly increases the exclusive-inclusive tension. Moreover, the current experimental results for the ratios of the $B \rightarrow D^{(*)} \tau \bar{\nu}$ and $B \rightarrow D^{(*)} \ell \bar{\nu}$ ($\ell = e, \mu$) branching fractions differ from the Standard-Model expectation with a combined significance of 3.4σ [14].

On the experimental front, new results are expected from the future Belle II detector at the SuperKEKB e^+e^- collider, and in the near future also from LHCb at the Large Hadron Collider. The LHCb Collaboration is currently analyzing the ratio of branching fractions of the baryonic $b \rightarrow u$ and $b \rightarrow c$ decays $\Lambda_b \rightarrow p \mu^- \bar{\nu}_\mu$ and $\Lambda_b \rightarrow \Lambda_c \mu^- \bar{\nu}_\mu$, with the aim of determining $|V_{ub}/V_{cb}|$ for the first time at a hadron collider. These decays were chosen over the more conventional $B \rightarrow \pi \mu \bar{\nu}$ and $B \rightarrow D \mu \bar{\nu}$ decays because, with the LHCb detector, final states containing protons are easier to identify than final states with pions [15]. Note that the production rate of Λ_b baryons at the LHC is remarkably high, equal to approximately 1/2 times the production rate of \bar{B}^0 mesons [16].

The extraction of $|V_{ub}|$ and $|V_{cb}|$ (or their ratio) from the measured $\Lambda_b \rightarrow p \mu^- \bar{\nu}_\mu$ and $\Lambda_b \rightarrow \Lambda_c \mu^- \bar{\nu}_\mu$ branching fractions requires knowledge of the form factors describing the $\Lambda_b \rightarrow p$ and $\Lambda_b \rightarrow \Lambda_c$ matrix elements of the relevant $b \rightarrow u$ and $b \rightarrow c$ currents in the weak effective Hamiltonian. These form factors have been studied using sum rules

* smeinel@email.arizona.edu

and quark models [17–28]. Nonperturbative QCD calculations of the $\Lambda_b \rightarrow p$ and $\Lambda_b \rightarrow \Lambda_c$ form factors can be performed using lattice gauge theory. The first lattice QCD calculation of $\Lambda_b \rightarrow p$ form factors, published in Ref. [29], employed static b quarks (i.e., leading-order heavy-quark effective theory) to simplify the analysis. The static limit reduces the number of independent $\Lambda_b \rightarrow p$ form factors to two [30–32], but introduces systematic uncertainties of order Λ_{QCD}/m_b and $|\mathbf{p}'|/m_b$ in the $\Lambda_b \rightarrow p \mu^- \bar{\nu}_\mu$ differential decay rate (where \mathbf{p}' is the momentum of the proton in the Λ_b rest frame). Here we present a new lattice calculation which improves upon Ref. [29] by replacing the static b quarks by relativistic b quarks, eliminating this systematic uncertainty. In addition to the six form factors describing the hadronic part of the decay $\Lambda_b \rightarrow p \mu^- \bar{\nu}_\mu$ in fully relativistic QCD, we also compute the six analogous form factors for $\Lambda_b \rightarrow \Lambda_c \mu^- \bar{\nu}_\mu$ (note that early lattice studies of $\Lambda_b \rightarrow \Lambda_c$ form factors in the quenched approximation can be found in Refs. [33, 34]). Preliminary results from the present work were shown in Ref. [35].

In Sec. II we provide the definitions of the form factors employed here. The lattice actions and parameters, as well as the matching of the $b \rightarrow u$ and $b \rightarrow c$ currents from the lattice renormalization scheme to the continuum $\overline{\text{MS}}$ scheme are discussed in Sec. III. This calculation is based on the same lattice gauge-field ensembles as Ref. [29]; the ensembles include 2+1 flavor of dynamical domain-wall fermions and were generated by the RBC and UKQCD Collaborations [36]. Section IV explains our method for extracting the form factors from ratios of three-point and two-point correlation functions and removing excited-state contamination by extrapolating to infinite source-sink separation. Our fits of the quark-mass, lattice-spacing, and momentum-dependence of the form factors are discussed in Sec. V. The form factors in the physical limit are presented in terms of z -expansion [37] parameters and their correlation matrices. Two different sets of parameters, referred to as the “nominal parameters” and the “higher-order parameters” are given. The nominal parameters are used to obtain the central values and statistical uncertainties of the form factors (and of derived quantities), while the higher-order parameters are used to calculate systematic uncertainties. In Sec. VI we then present predictions for the $\Lambda_b \rightarrow p \ell^- \bar{\nu}_\ell$ and $\Lambda_b \rightarrow \Lambda_c \ell^- \bar{\nu}_\ell$ differential and integrated decay rates using our form factors. Combined with experimental data, our results for the $\Lambda_b \rightarrow p \mu^- \bar{\nu}_\mu$ and $\Lambda_b \rightarrow \Lambda_c \mu^- \bar{\nu}_\mu$ decay rates in the high- q^2 region will allow determinations of $|V_{ub}|$ and $|V_{cb}|$ with theory uncertainties of 4.4% and 2.2%, respectively.

II. DEFINITIONS OF THE FORM FACTORS

Allowing for possible right-handed currents beyond the Standard Model, the effective weak Hamiltonian for $b \rightarrow q \ell^- \bar{\nu}_\ell$ transitions (where $q = u, c$) can be written as

$$\mathcal{H}_{\text{eff}} = \frac{G_F}{\sqrt{2}} V_{qb}^L [(1 + \epsilon_q^R) \bar{q} \gamma^\mu b - (1 - \epsilon_q^R) \bar{q} \gamma^\mu \gamma_5 b] \bar{\ell} \gamma_\mu (1 - \gamma_5) \nu \quad (2)$$

(in the Standard Model, $\epsilon_q^R = 0$ and $V_{qb}^L = V_{qb}$). To calculate the differential decay rate and other observables, we therefore need the hadronic matrix elements of the vector and axial vector currents, $\bar{q} \gamma^\mu b$ and $\bar{q} \gamma^\mu \gamma_5 b$. In the following, we denote the final-state baryon by X ($X = p, \Lambda_c$). Lorentz and discrete symmetries imply that the matrix elements $\langle X | \bar{q} \gamma^\mu b | \Lambda_b \rangle$ and $\langle X | \bar{q} \gamma^\mu \gamma_5 b | \Lambda_b \rangle$ can each be decomposed into three form factors. In this work we primarily use a helicity-based definition of the $\Lambda_b \rightarrow X$ form factors, which was introduced in Ref. [38] and is given by

$$\begin{aligned} \langle X(p', s') | \bar{q} \gamma^\mu b | \Lambda_b(p, s) \rangle &= \bar{u}_X(p', s') \left[f_0(q^2) (m_{\Lambda_b} - m_X) \frac{q^\mu}{q^2} \right. \\ &\quad + f_+(q^2) \frac{m_{\Lambda_b} + m_X}{s_+} \left(p^\mu + p'^\mu - (m_{\Lambda_b}^2 - m_X^2) \frac{q^\mu}{q^2} \right) \\ &\quad \left. + f_\perp(q^2) \left(\gamma^\mu - \frac{2m_X}{s_+} p^\mu - \frac{2m_{\Lambda_b}}{s_+} p'^\mu \right) \right] u_{\Lambda_b}(p, s), \end{aligned} \quad (3)$$

$$\begin{aligned} \langle X(p', s') | \bar{q} \gamma^\mu \gamma_5 b | \Lambda_b(p, s) \rangle &= -\bar{u}_X(p', s') \gamma_5 \left[g_0(q^2) (m_{\Lambda_b} + m_X) \frac{q^\mu}{q^2} \right. \\ &\quad + g_+(q^2) \frac{m_{\Lambda_b} - m_X}{s_-} \left(p^\mu + p'^\mu - (m_{\Lambda_b}^2 - m_X^2) \frac{q^\mu}{q^2} \right) \\ &\quad \left. + g_\perp(q^2) \left(\gamma^\mu + \frac{2m_X}{s_-} p^\mu - \frac{2m_{\Lambda_b}}{s_-} p'^\mu \right) \right] u_{\Lambda_b}(p, s). \end{aligned} \quad (4)$$

In these expressions, $q = p - p'$ is the four-momentum transfer (whereas \bar{q} is the \bar{u} or \bar{c} quark field), and s_\pm is defined as

$$s_\pm = (m_{\Lambda_b} \pm m_X)^2 - q^2. \quad (5)$$

The form factors with subscripts 0, +, \perp describe the contractions of the above matrix elements with virtual polarization vectors ϵ_μ^* that are, respectively, time-like, longitudinal, and transverse to q^μ . Consequently, this choice of form factors leads to particularly simple expressions for observables such as the differential decay rate. Moreover, this choice simplifies the extraction of the form factors from correlation functions and clarifies the spin-parity quantum numbers of poles outside the physical kinematic region $0 \leq q^2 \leq (m_{\Lambda_b} - m_X)^2$.

An alternate definition of the form factors that can be found in the literature (see, e.g., Ref. [27]) is the following:

$$\langle X(p', s') | \bar{q} \gamma^\mu b | \Lambda_b(p) \rangle = \bar{u}_X(p', s') \left[f_1^V(q^2) \gamma^\mu - \frac{f_2^V(q^2)}{m_{\Lambda_b}} i \sigma^{\mu\nu} q_\nu + \frac{f_3^V(q^2)}{m_{\Lambda_b}} q^\mu \right] u_{\Lambda_b}(p, s), \quad (6)$$

$$\langle X(p', s') | \bar{q} \gamma^\mu \gamma_5 b | \Lambda_b(p) \rangle = \bar{u}_X(p', s') \left[f_1^A(q^2) \gamma^\mu - \frac{f_2^A(q^2)}{m_{\Lambda_b}} i \sigma^{\mu\nu} q_\nu + \frac{f_3^A(q^2)}{m_{\Lambda_b}} q^\mu \right] \gamma_5 u_{\Lambda_b}(p, s), \quad (7)$$

where $\sigma^{\mu\nu} = \frac{i}{2}(\gamma^\mu \gamma^\nu - \gamma^\nu \gamma^\mu)$ and, as before, $q = p - p'$. This choice decomposes the matrix elements into form factors of the first and second class according to Weinberg's classification [39]. The second-class form factors f_3^V and f_3^A would vanish in the limit $m_b = m_c$ (for $\Lambda_b \rightarrow \Lambda_c$) or $m_b = m_u$ (for $\Lambda_b \rightarrow p$) [40]. In the following, we will refer to the form factors defined in Eqs. (6), (7) as ‘‘Weinberg form factors’’. The helicity form factors are related to the Weinberg form factors as follows:

$$f_+(q^2) = f_1^V(q^2) + \frac{q^2}{m_{\Lambda_b}(m_{\Lambda_b} + m_X)} f_2^V(q^2), \quad (8)$$

$$f_\perp(q^2) = f_1^V(q^2) + \frac{m_{\Lambda_b} + m_X}{m_{\Lambda_b}} f_2^V(q^2), \quad (9)$$

$$f_0(q^2) = f_1^V(q^2) + \frac{q^2}{m_{\Lambda_b}(m_{\Lambda_b} - m_X)} f_3^V(q^2), \quad (10)$$

$$g_+(q^2) = f_1^A(q^2) - \frac{q^2}{m_{\Lambda_b}(m_{\Lambda_b} - m_X)} f_2^A(q^2), \quad (11)$$

$$g_\perp(q^2) = f_1^A(q^2) - \frac{m_{\Lambda_b} - m_X}{m_{\Lambda_b}} f_2^A(q^2), \quad (12)$$

$$g_0(q^2) = f_1^A(q^2) - \frac{q^2}{m_{\Lambda_b}(m_{\Lambda_b} + m_X)} f_3^A(q^2). \quad (13)$$

These relations also demonstrate the following endpoint constraints for the helicity form factors:

$$f_0(0) = f_+(0), \quad (14)$$

$$g_0(0) = g_+(0), \quad (15)$$

$$g_\perp(q_{\max}^2) = g_+(q_{\max}^2), \quad (16)$$

where $q_{\max}^2 = (m_{\Lambda_b} - m_X)^2$. At intermediate stages of our analysis of the lattice QCD data, it is beneficial to work with both definitions of the form factors. However, we perform the chiral/continuum/kinematic extrapolations only in the helicity basis.

III. LATTICE ACTIONS AND CURRENTS

This calculation is based on lattice gauge field ensembles generated by the RBC and UKQCD collaborations [36] with the Iwasaki gauge action [41, 42] and 2+1 flavors of dynamical domain-wall fermions [43–45]. We implement the light (u or d) valence quarks with the same domain-wall action that was used in generating the ensembles. Our analysis uses six different combinations of light-quark masses and lattice spacings as shown in Table I. These parameters are identical to those used in the earlier calculation of $\Lambda_b \rightarrow p \ell \bar{\nu}$ form factors in Ref. [29]. However, instead of the static Eichten-Hill action [46] employed in Ref. [29], we now use anisotropic clover actions for the heavy (c and b) quarks [47–50]. These actions have the form

$$S_Q = a^4 \sum_x \bar{Q} \left[m_Q + \gamma_0 \nabla_0 - \frac{a}{2} \nabla_0^{(2)} + \nu \sum_{i=1}^3 \left(\gamma_i \nabla_i - \frac{a}{2} \nabla_i^{(2)} \right) - c_E \frac{a}{2} \sum_{i=1}^3 \sigma_{0i} F_{0i} - c_B \frac{a}{4} \sum_{i,j=1}^3 \sigma_{ij} F_{ij} \right] Q, \quad (17)$$

where Q is the lattice charm or bottom quark field, ∇_μ and $\nabla_\mu^{(2)}$ are first- and second-order covariant lattice derivatives, and $F_{\mu\nu}$ is a lattice expression for the field-strength tensor (all of which are defined as in Ref. [51]). By suitably tuning

Set	β	$N_s^3 \times N_t \times N_5$	am_5	$am_s^{(\text{sea})}$	$am_{u,d}^{(\text{sea})}$	a (fm)	$am_{u,d}^{(\text{val})}$	$m_\pi^{(\text{val})}$ (MeV)	N_{meas}
C14	2.13	$24^3 \times 64 \times 16$	1.8	0.04	0.005	0.1119(17)	0.001	245(4)	2672
C24	2.13	$24^3 \times 64 \times 16$	1.8	0.04	0.005	0.1119(17)	0.002	270(4)	2676
C54	2.13	$24^3 \times 64 \times 16$	1.8	0.04	0.005	0.1119(17)	0.005	336(5)	2782
F23	2.25	$32^3 \times 64 \times 16$	1.8	0.03	0.004	0.0849(12)	0.002	227(3)	1907
F43	2.25	$32^3 \times 64 \times 16$	1.8	0.03	0.004	0.0849(12)	0.004	295(4)	1917
F63	2.25	$32^3 \times 64 \times 16$	1.8	0.03	0.006	0.0848(17)	0.006	352(7)	2782

TABLE I. Parameters of the lattice gauge field ensembles [36] and light-quark propagators [29, 53]. The three groups of data sets {C14, C24, C54}, {F23, F43}, and {F63} correspond to three different ensembles of lattice gauge fields: one with a “coarse” lattice spacing $a \approx 0.11$ fm, and two with “fine” lattice spacings $a \approx 0.085$ fm (we use the lattice spacing values determined in Ref. [54]). Within each group, the valence-quark masses $am_{u,d}^{(\text{val})}$ used for the propagators differ, resulting in different “valence pion masses” $m_\pi^{(\text{val})}$; the number of light-quark propagators used in each data set is denoted as N_{meas} .

Parameter	coarse	fine
$am_Q^{(b)}$	8.45	3.99
$\xi^{(b)}$	3.1	1.93
$c_{E,B}^{(b)}$	5.8	3.57
$am_Q^{(c)}$	0.1214	-0.0045
$\xi^{(c)}$	1.2362	1.1281
$c_E^{(c)}$	1.6650	1.5311
$c_B^{(c)}$	1.8409	1.6232

TABLE II. Parameters of the bottom and charm quark actions [51, 52].

the parameters ν , c_E , c_B as functions of am_Q , heavy-quark discretization errors proportional to powers of am_Q can be removed to all orders. The remaining discretization errors are of order $a^2|\mathbf{p}|^2$, where $|\mathbf{p}|$ is the typical magnitude of the spatial momentum of the heavy quark inside the hadron. As the continuum limit $a \rightarrow 0$ is approached, the values $\nu = 1$ and $c_E = c_B = c_{\text{SW}}$ corresponding to the standard clover-improved Wilson action are recovered. For the bottom quark, we use the parameters that were tuned nonperturbatively by the RBC and UKQCD collaborations [51] using the condition that the action reproduces the correct spin-averaged B_s meson mass and relativistic dispersion relation, as well as the correct $B_s^* - B_s$ hyperfine splitting. For the charm quarks, we use the parameters from Ref. [52], where am_Q and ν were tuned nonperturbatively to obtain the correct spin-averaged charmonium mass and relativistic dispersion relation, while c_E and c_B were set to mean-field improved tree-level predictions. Note that after the parameters were tuned in this way, the calculated charmonium hyperfine splittings were also in agreement with experiment [52]. The values of all heavy-quark action parameters used here are given in Table II.

We use a mostly nonperturbative method [55, 56] to match the $b \rightarrow q$ ($q = u, c$) vector and axial vector currents from the lattice scheme to the continuum $\overline{\text{MS}}$ scheme. The renormalized currents in the $\overline{\text{MS}}$ scheme are written in terms of the lattice quark and gluon fields as

$$V_0 = \sqrt{Z_V^{(qq)} Z_V^{(bb)}} \rho_{V_0} \left[\bar{q} \gamma_0 b + 2a \left(c_{V_0}^R \bar{q} \gamma_0 \gamma_j \vec{\nabla}_j b + c_{V_0}^L \bar{q} \overleftarrow{\nabla}_j \gamma_0 \gamma_j b \right) \right], \quad (18)$$

$$A_0 = \sqrt{Z_V^{(qq)} Z_V^{(bb)}} \rho_{A_0} \left[\bar{q} \gamma_0 \gamma_5 b + 2a \left(c_{A_0}^R \bar{q} \gamma_0 \gamma_5 \gamma_j \vec{\nabla}_j b + c_{A_0}^L \bar{q} \overleftarrow{\nabla}_j \gamma_0 \gamma_5 \gamma_j b \right) \right], \quad (19)$$

$$V_i = \sqrt{Z_V^{(qq)} Z_V^{(bb)}} \rho_{V_i} \left[\bar{q} \gamma_i b + 2a \left(c_{V_i}^R \bar{q} \gamma_i \gamma_j \vec{\nabla}_j b + c_{V_i}^L \bar{q} \overleftarrow{\nabla}_j \gamma_i \gamma_j b + d_{V_i}^R \bar{q} \vec{\nabla}_i b + d_{V_i}^L \bar{q} \overleftarrow{\nabla}_i b \right) \right], \quad (20)$$

$$A_i = \sqrt{Z_V^{(qq)} Z_V^{(bb)}} \rho_{A_i} \left[\bar{q} \gamma_i \gamma_5 b + 2a \left(c_{A_i}^R \bar{q} \gamma_i \gamma_5 \gamma_j \vec{\nabla}_j b + c_{A_i}^L \bar{q} \overleftarrow{\nabla}_j \gamma_i \gamma_5 \gamma_j b + d_{A_i}^R \bar{q} \gamma_5 \vec{\nabla}_i b + d_{A_i}^L \bar{q} \overleftarrow{\nabla}_i \gamma_5 b \right) \right], \quad (21)$$

where $Z_V^{(qq)}$ and $Z_V^{(bb)}$ are the matching factors of the flavor-conserving temporal vector currents $\bar{q} \gamma_0 q$ and $\bar{b} \gamma_0 b$, which are computed nonperturbatively using charge conservation. These nonperturbative factors provide the bulk of the renormalization, resulting in a much improved convergence of perturbation theory for the residual matching factors ρ_{V_μ, A_μ} . Above, i denotes the spatial components ($i = 1, 2, 3$), and the repeated index j is summed from 1 to 3. The

Parameter	$b \rightarrow c$, coarse	$b \rightarrow c$, fine	$b \rightarrow u$, coarse	$b \rightarrow u$, fine
ρ_{V^0}	0.9798(20)	0.9848(15)	1.02658(69)	1.01661(52)
ρ_{A^0}	1.0193(15)	1.0112(29)	1.02658(69)	1.01661(52)
ρ_{V^j}	1.0184(38)	1.0162(41)	0.99723(25)	0.99398(12)
ρ_{A^j}	0.9866(33)	0.9896(26)	0.99723(25)	0.99398(12)
$c_{V^0}^R$	0.0258(13)	0.02873(99)	0.0558(63)	0.0547(64)
$c_{A^0}^R$	0.03500(93)	0.03285(87)	0.0558(63)	0.0547(64)
$c_{V^0}^L$	-0.0183(32)	-0.0135(22)	-0.0099(99)	-0.0095(95)
$c_{A^0}^L$	-0.0205(17)	-0.0155(27)	-0.0099(99)	-0.0095(95)
$c_{V^j}^R$	0.03192(70)	0.0305(10)	0.0485(27)	0.0480(30)
$c_{A^j}^R$	0.0221(31)	0.0237(20)	0.0485(27)	0.0480(30)
$c_{V^j}^L$	0.0088(22)	0.0027(35)	-0.0033(33)	-0.0020(20)
$c_{A^j}^L$	-0.0002(31)	-0.0020(20)	-0.0033(33)	-0.0020(20)
$d_{V^j}^R$	-0.0055(12)	-0.0067(17)	-0.00079(79)	-0.0012(12)
$d_{A^j}^R$	0.0060(69)	0.0044(40)	0.00079(79)	0.0012(12)
$d_{V^j}^L$	-0.0176(44)	-0.0043(69)	0.0018(18)	0.00047(48)
$d_{A^j}^L$	0.0134(69)	0.0106(40)	-0.0018(18)	-0.00047(48)

TABLE III. Perturbative renormalization and improvement coefficients. The uncertainties given here include estimates of the missing higher-loop corrections as well as uncertainties from the numerical evaluation of the one-loop integrals. They are explained in more detail in the main text.

lattice currents containing the lattice derivatives

$$\vec{\nabla}_\mu b = \frac{1}{2a} [U_\mu(x)b(x + \hat{\mu}) - U_\mu^\dagger(x - \hat{\mu})b(x - \hat{\mu})], \quad (22)$$

$$\bar{q} \overleftarrow{\nabla}_\mu = \frac{1}{2a} [\bar{q}(x + \hat{\mu})U_\mu^\dagger(x) - \bar{q}(x - \hat{\mu})U_\mu(x - \hat{\mu})], \quad (23)$$

are needed to remove $\mathcal{O}(a)$ -discretization errors from the currents. Time derivatives have been eliminated in Eqs. (18–21) using the equations of motion. We have computed ρ_{V_μ, A_μ} as well as all of the $\mathcal{O}(a)$ -improvement coefficients $c_{V_\mu, A_\mu}^{R,L}$, $d_{V_\mu, A_\mu}^{R,L}$ to one loop in mean-field improved lattice perturbation theory using the automated framework `PhySyHCA1` [57, 58]. The results are given in Table III. The central values are the average of plaquette and Landau-gauge mean-field improved results with perturbative expansion in $\alpha_{\overline{\text{MS}}}(\mu = a^{-1})$ [51]. The uncertainties are the maximum of i) the difference of the respective mean-field improved results, ii) the numerical integration error, and iii) a power-counting estimate. For consistency with earlier stages of this project a different power-counting estimate is used for the $b \rightarrow u$ and $b \rightarrow c$ cases. For a perturbative quantity h with tree-level result $h^{(0)}$ and full one-loop result $h^{(1)}$ we use $(h^{(0)}/h^{(1)} - 1)^2 h^{(1)}$ as an error estimate for $b \rightarrow u$ and $(h^{(1)} - h^{(0)}) (\alpha_{\overline{\text{MS}}}(\mu = a^{-1})/\pi)$ as an estimate for $b \rightarrow c$. For the ρ factors (but not for the $\mathcal{O}(a)$ -improvement coefficients) this estimate tends to be less conservative than estimates that are used in similar work [11, 12, 59]. The estimates of the combined uncertainty from the ρ factors and $\mathcal{O}(a)$ -improvement coefficients, see Figs. 11, 13 and Table XII, agree well with similar work [11, 12, 59].

The nonperturbative matching factors $Z_V^{(qa)}$ and $Z_V^{(bb)}$ are given in Table IV. The light-quark and bottom-quark $Z_V^{(uu)}$ and $Z_V^{(bb)}$ were computed by the RBC and UKQCD collaborations [36, 60]. We determined the charm-quark $Z_V^{(cc)}$ using the method of Ref. [60], by computing the following ratio of D_s meson correlation functions without and with insertion of the current $J_0 = \bar{c}\gamma_0 c$:

$$R_{Z_V^{(cc)}}(t, t') = \frac{\sum_{\mathbf{z}} \langle D_s(x_0 + t, \mathbf{z}) D_s^\dagger(x_0, \mathbf{x}) \rangle}{\sum_{\mathbf{y}, \mathbf{z}} \langle D_s(x_0 + t, \mathbf{z}) J_0(x_0 + t', \mathbf{y}) D_s^\dagger(x_0, \mathbf{x}) \rangle}. \quad (24)$$

Here, we used the following interpolating field with the quantum numbers of the D_s meson,

$$D_s = \bar{s}\gamma_5 \tilde{c}, \quad (25)$$

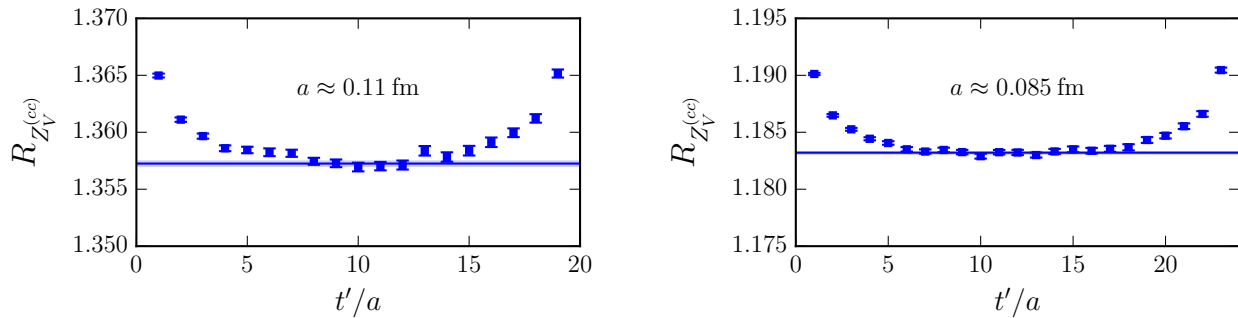


FIG. 1. Numerical results for the ratio $R_{Z_V^{(cc)}}(t, t')$ at $t/a = 20$ for the C54 data set (left) and at $t/a = 24$ for the F43 data set (right). The horizontal lines indicate the extracted values of $Z_V^{(cc)}$.

Parameter	coarse	fine
$Z_V^{(bb)}$	10.037(34)	5.270(13)
$Z_V^{(cc)}$	1.35725(23)	1.18321(14)
$Z_V^{(uu)}$	0.71651(46)	0.74475(12)

TABLE IV. Nonperturbative renormalization factors of the flavor-conserving temporal vector currents. For $Z_V^{(uu)}$, we use the results in the chiral limit from Ref. [36]. For $Z_V^{(bb)}$, we use the results obtained in Ref. [60] on the coarse $am_{u,d}^{(\text{sea})} = 0.005$ and fine $am_{u,d}^{(\text{sea})} = 0.004$ ensembles.

where the tilde indicates gauge-covariant Gaussian smearing to suppress excited-state contamination. For large Euclidean time separations t , t' , and $|t - t'|$, the ratio (24) becomes equal to $Z_V^{(cc)}$. Our numerical results for $R_{Z_V^{(cc)}}(t, t')$, along with fits in the plateau region giving $Z_V^{(cc)}$, are shown in Fig. 1 for the ensembles used in this calculation.

IV. EXTRACTION OF THE FORM FACTORS FROM CORRELATION FUNCTIONS

In this section we explain how we extract the form factors at the different lattice spacings and quark masses from nonperturbative Euclidean correlation functions. The extrapolations of these results to the physical limit will be discussed in Sec. V.

We use the following interpolating fields for the Λ_b , Λ_c , and the proton,

$$\Lambda_{b\alpha} = \epsilon^{abc} (C\gamma_5)_{\beta\gamma} \tilde{d}_\beta^a \tilde{u}_\gamma^b \tilde{b}_\alpha^c, \quad (26)$$

$$\Lambda_{c\alpha} = \epsilon^{abc} (C\gamma_5)_{\beta\gamma} \tilde{d}_\beta^a \tilde{u}_\gamma^b \tilde{c}_\alpha^c, \quad (27)$$

$$N_\alpha = \epsilon^{abc} (C\gamma_5)_{\beta\gamma} \tilde{u}_\beta^a \tilde{d}_\gamma^b \tilde{u}_\alpha^c, \quad (28)$$

where C is the charge-conjugation matrix, a, b, c are color indices, and α, β, γ are spinor indices (the symbol N is used for the proton to avoid confusion with the Λ_b -momentum p). The tilde on the quark fields indicates gauge-covariant Gaussian smearing. For the u and d quarks, the smearing parameters are the same as in Ref. [61]. In the notation of Ref. [61], for the charm quarks we used $(\sigma, n_S) = (3.0, 70)$ at the coarse lattice spacing and $(\sigma, n_S) = (4.0, 70)$ at the fine lattice spacing, and for the bottom quarks $(\sigma, n_S) = (2.0, 10)$ at the coarse lattice spacing and $(\sigma, n_S) = (2.67, 10)$ at the fine lattice spacing. The smearing of both the charm and bottom quark fields was done using Stout-smear gauge links [62] with ten iterations and staple weight $\rho = 0.08$ in the spatial directions.

In the following, we denote the final-state interpolating field by $X_\alpha (= N_\alpha, \Lambda_{c\alpha})$ and the renormalized currents as J_Γ , where

$$J_{\gamma\mu} = V_\mu, \quad (29)$$

$$J_{\gamma\mu\gamma_5} = A_\mu, \quad (30)$$

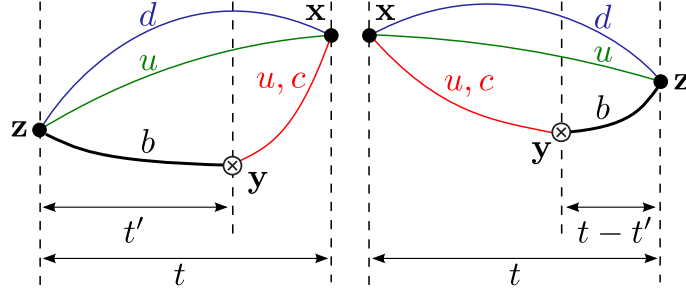


FIG. 2. Illustration of the quark field contractions on a given background gauge field for the forward (left) and backward (right) three-point functions. The u , d , and c quark propagators are common to the forward and backward three-point functions and have a Gaussian-smeared source at (x_0, \mathbf{x}) . We sum over the spatial points \mathbf{x} and \mathbf{y} with the appropriate phases to project to definite momenta. The b -quark propagators are computed using the sequential source method, with sequential sources on the time slices $x_0 \pm t$.

with V_μ and A_μ given by Eqs. (18-21). We set the Λ_b three-momentum \mathbf{p} to zero, and compute “forward” and “backward” three-point functions (where $t \geq t' \geq 0$),

$$C_{\delta\alpha}^{(3,\text{fw})}(\Gamma, \mathbf{p}', t, t') = \sum_{\mathbf{y}, \mathbf{z}} e^{-i\mathbf{p}' \cdot (\mathbf{x}-\mathbf{y})} \langle X_\delta(x_0, \mathbf{x}) \quad J_\Gamma^\dagger(x_0 - t + t', \mathbf{y}) \quad \bar{\Lambda}_{b\alpha}(x_0 - t, \mathbf{z}) \rangle, \quad (31)$$

$$C_{\alpha\delta}^{(3,\text{bw})}(\Gamma, \mathbf{p}', t, t-t') = \sum_{\mathbf{y}, \mathbf{z}} e^{-i\mathbf{p}' \cdot (\mathbf{y}-\mathbf{x})} \langle \Lambda_{b\alpha}(x_0 + t, \mathbf{z}) \quad J_\Gamma(x_0 + t', \mathbf{y}) \quad \bar{X}_\delta(x_0, \mathbf{x}) \rangle, \quad (32)$$

as well as the two-point functions

$$C_{\delta\alpha}^{(2,X,\text{fw})}(\mathbf{p}', t) = \sum_{\mathbf{y}} e^{-i\mathbf{p}' \cdot (\mathbf{y}-\mathbf{x})} \langle X_\delta(x_0 + t, \mathbf{y}) \bar{X}_\alpha(x_0, \mathbf{x}) \rangle, \quad (33)$$

$$C_{\delta\alpha}^{(2,X,\text{bw})}(\mathbf{p}', t) = \sum_{\mathbf{y}} e^{-i\mathbf{p}' \cdot (\mathbf{x}-\mathbf{y})} \langle X_\delta(x_0, \mathbf{x}) \bar{X}_\alpha(x_0 - t, \mathbf{y}) \rangle, \quad (34)$$

$$C_{\delta\alpha}^{(2,\Lambda_b,\text{fw})}(t) = \sum_{\mathbf{y}} \langle \Lambda_{b\delta}(x_0 + t, \mathbf{y}) \bar{\Lambda}_{b\alpha}(x_0, \mathbf{x}) \rangle, \quad (35)$$

$$C_{\delta\alpha}^{(2,\Lambda_b,\text{bw})}(t) = \sum_{\mathbf{y}} \langle \Lambda_{b\delta}(x_0, \mathbf{x}) \bar{\Lambda}_{b\alpha}(x_0 - t, \mathbf{y}) \rangle. \quad (36)$$

These definitions are similar to those in the static b -quark case [29, 53], but with the relativistic heavy-quark action used here, the b quark can propagate in all directions, and we included additional sums over the spatial coordinates for the momentum projections. The quark-field contractions for the three-point functions are illustrated in Fig. 2. Only the b -quark sequential propagators need to be recomputed for each source-sink separation, t . For the proton final state, 16 times as many sequential propagators are needed as for the Λ_c final state because of the different structure of diquark contractions. The b -quark propagators decay extremely fast with distance, and care has to be taken to perform sufficiently many conjugate-gradient iterations to get an accurate solution up to the distance needed.

We computed the three-point functions for all final-state momenta \mathbf{p}' with $|\mathbf{p}'|^2 \leq 12(2\pi/L)^2$, and for the ranges of source-sink separations shown in Table V. In a first run we computed the three-point functions for all possible values of t/a in the wide ranges shown in the left column of Table V, but only for the lattice currents of the form $\bar{q}\Gamma b$ and $\bar{q}\Gamma \gamma_j \vec{\nabla}_j b$. In a second run, we then computed the three-point functions for all of the remaining $\mathcal{O}(a)$ -improvement currents shown in Eqs. (18-21), but only for the subsets of separations in the right column of Table V to save computer time and disk space. For one of the data sets (C14), we performed the calculation of all the currents for the whole range of source-sink separations. As shown in Fig. 4, the effects of the additional $\mathcal{O}(a)$ improvements are small. Our method for effectively including these corrections for all source-sink separations will be explained further below.

To discuss the spectral decomposition of the correlation functions, we introduce the overlap factors

$$\langle 0 | \Lambda_{b\alpha}(0) | \Lambda_b(p, s) \rangle = [(Z_{\Lambda_b}^{(1)} + Z_{\Lambda_b}^{(2)} \gamma^0) u(p, s)]_\alpha, \quad (37)$$

$$\langle 0 | X_\alpha(0) | X(p', s') \rangle = [(Z_X^{(1)} + Z_X^{(2)} \gamma^0) u(p', s')]_\alpha. \quad (38)$$

The two separate Z factors for each matrix element are needed because the spatial-only smearing of the quark fields in the interpolating field breaks hypercubic symmetry [33]. Because we set $\mathbf{p} = 0$, we can write

$$\langle 0 | \Lambda_{b\alpha}(0) | \Lambda_p(p, s) \rangle = Z_{\Lambda_b} u(p, s)_\alpha, \quad (39)$$

Set	Partial $\mathcal{O}(a)$ -improvement	Full $\mathcal{O}(a)$ -improvement
C14	$t/a = 4 \dots 15$	$t/a = 4 \dots 15$
C24	$t/a = 4 \dots 15$	$t/a = 5, 8, 11$
C54	$t/a = 4 \dots 15$	$t/a = 5, 8, 11$
F23	$t/a = 5 \dots 15$	$t/a = 6, 10, 14$
F43	$t/a = 5 \dots 15$	$t/a = 6, 10, 14$
F63	$t/a = 5 \dots 17$	$t/a = 6, 10, 14$

TABLE V. Source-sink separations used for the three-point functions for each data set. For the separations in the column “full $\mathcal{O}(a)$ -improvement”, we computed the three-point functions for all of the $\mathcal{O}(a)$ -corrections in Eqs. (18-21). For the separations in the column “partial $\mathcal{O}(a)$ -improvement”, we computed only the corrections with coefficients $c_{V_\mu}^R$ and $c_{A_\mu}^R$. As explained in the main text and illustrated in Fig. 4, the effects of the missing terms are very small and practically independent of the source-sink separation, and we achieve full $\mathcal{O}(a)$ -improvement for all separations by applying t -independent correction factors computed using the subsets of separations where all $\mathcal{O}(a)$ -corrections are available.

where $Z_{\Lambda_b} = Z_{\Lambda_b}^{(1)} + Z_{\Lambda_b}^{(2)}$. Further, we introduce the following short-hand notation for the form factor decomposition of the matrix elements (cf. Sec. II):

$$\langle X(p', s') | J_\Gamma | \Lambda_b(p, s) \rangle = \bar{u}_X(p', s') \mathcal{G}[\Gamma] u_{\Lambda_b}(p, s). \quad (40)$$

The spectral decompositions of the correlation functions then read

$$C^{(3,\text{fw})}(\mathbf{p}', \Gamma, t, t') = Z_{\Lambda_b} \frac{1}{2E_X} \frac{1}{2m_{\Lambda_b}} e^{-E_X(t-t')} e^{-m_{\Lambda_b}t'} \left[(Z_X^{(1)} + Z_X^{(2)}\gamma^0)(m_X + \not{p}') \mathcal{G}[\Gamma] m_{\Lambda_b}(1 + \gamma^0) \right] \\ + (\text{excited-state contributions}), \quad (41)$$

$$C^{(3,\text{bw})}(\mathbf{p}', \Gamma, t, t-t') = Z_{\Lambda_b} \frac{1}{2E_X} \frac{1}{2m_{\Lambda_b}} e^{-m_{\Lambda_b}(t-t')} e^{-E_X t'} \left[m_{\Lambda_b}(1 + \gamma^0) \overline{\mathcal{G}[\Gamma]} (m_X + \not{p}') (Z_X^{(1)} + Z_X^{(2)}\gamma^0) \right] \\ + (\text{excited-state contributions}), \quad (42)$$

$$C^{(2,X,\text{fw})}(\mathbf{p}', t) = C^{(2,X,\text{bw})}(\mathbf{p}', t) = \frac{1}{2E_X} e^{-E_X t} \left[(Z_X^{(1)} + Z_X^{(2)}\gamma^0)(m_X + \not{p}') (Z_X^{(1)} + Z_X^{(2)}\gamma^0) \right] \\ + (\text{excited-state contributions}), \quad (43)$$

$$C^{(2,\Lambda_b,\text{fw})}(t) = C^{(2,\Lambda_b,\text{bw})}(t) = \frac{1}{2m_{\Lambda_b}} e^{-m_{\Lambda_b}t} \left[Z_{\Lambda_b}^2 m_{\Lambda_b}(1 + \gamma^0) \right] \\ + (\text{excited-state contributions}), \quad (44)$$

where $\overline{\mathcal{G}[\Gamma]} = \gamma_0 \mathcal{G}[\Gamma]^\dagger \gamma_0$, and all correlators are 4×4 matrices in spinor space. In the above expressions, we have explicitly shown only the ground-state contributions, which correspond to the positive-parity baryons of interest. The excited-state contributions decay exponentially faster with the time separations t', t .

To extract individual form factors, we contract the currents in the three-point functions with suitable polarization vectors and form certain double ratios that eliminate all the time-dependence and overlap factors for the ground-state contributions. For an arbitrary four-vector n , we define

$$r[n] = n - \frac{(q \cdot n)}{q^2} q, \quad (45)$$

where $q = p - p'$ is the four-momentum transfer. By construction, $r[n]$ is orthogonal to q . For the vector current, we define the three ratios

$$\mathcal{R}_+^V(\mathbf{p}', t, t') = \frac{r_\mu[(1, \mathbf{0})] r_\nu[(1, \mathbf{0})] \text{Tr} \left[C^{(3,\text{fw})}(\mathbf{p}', \gamma^\mu, t, t') C^{(3,\text{bw})}(\mathbf{p}', \gamma^\nu, t, t-t') \right]}{\text{Tr} \left[C^{(2,X,\text{av})}(\mathbf{p}', t) \right] \text{Tr} \left[C^{(2,\Lambda_b,\text{av})}(t) \right]}, \quad (46)$$

$$\mathcal{R}_\perp^V(\mathbf{p}', t, t') = \frac{r_\mu[(0, \mathbf{e}_j \times \mathbf{p}')] r_\nu[(0, \mathbf{e}_k \times \mathbf{p}')] \text{Tr} \left[C^{(3,\text{fw})}(\mathbf{p}', \gamma^\mu, t, t') \gamma_5 \gamma^j C^{(3,\text{bw})}(\mathbf{p}', \gamma^\nu, t, t-t') \gamma_5 \gamma^k \right]}{\text{Tr} \left[C^{(2,X,\text{av})}(\mathbf{p}', t) \right] \text{Tr} \left[C^{(2,\Lambda_b,\text{av})}(t) \right]}, \quad (47)$$

$$\mathcal{R}_0^V(\mathbf{p}', t, t') = \frac{q_\mu q_\nu \text{Tr} \left[C^{(3,\text{fw})}(\mathbf{p}', \gamma^\mu, t, t') C^{(3,\text{bw})}(\mathbf{p}', \gamma^\nu, t, t-t') \right]}{\text{Tr} \left[C^{(2,X,\text{av})}(\mathbf{p}', t) \right] \text{Tr} \left[C^{(2,\Lambda_b,\text{av})}(t) \right]}, \quad (48)$$

Set	am_{Λ_b}	am_{Λ_c}	am_N	am_{B_c}	am_B
C14	3.305(11)	1.3499(51)	0.6184(76)	3.60327(42)	3.0649(27)
C24	3.299(10)	1.3526(57)	0.6259(57)	3.60312(45)	3.0628(29)
C54	3.3161(71)	1.3706(40)	0.6580(39)	3.60326(44)	3.0638(33)
F23	2.469(16)	1.008(12)	0.4510(86)	2.73156(44)	2.3198(32)
F43	2.492(11)	1.0185(67)	0.4705(42)	2.73169(44)	2.3230(26)
F63	2.5089(70)	1.0314(40)	0.5004(25)	2.73257(33)	2.3221(22)

TABLE VI. Hadron masses in lattice units.

where \mathbf{e}_j is the three-dimensional unit vector in j -direction, and \times is the three-dimensional vector cross product. We sum over repeated indices μ, ν from 0 to 3 and over repeated indices j, k from 1 to 3. The quantities $C^{(2, \Lambda_b, \text{av})}$ and $C^{(2, X, \text{av})}$ in the denominators are the averages of the forward- and backward two-point functions.

These ratios are designed to isolate particular helicity form factors and are equal to

$$\mathcal{R}_+^V(\mathbf{p}', t, t') = \frac{(E_X - m_X)^2 (E_X + m_X) [m_{\Lambda_b} (m_{\Lambda_b} + m_X) f_+]^2}{4 m_{\Lambda_b}^2 E_X q^4} + (\text{excited-state contributions}), \quad (49)$$

$$\mathcal{R}_\perp^V(\mathbf{p}', t, t') = \frac{(E_X - m_X)^2 (E_X + m_X) [m_{\Lambda_b} f_\perp]^2}{m_{\Lambda_b}^2 E_X} + (\text{excited-state contributions}), \quad (50)$$

$$\mathcal{R}_0^V(\mathbf{p}', t, t') = \frac{(E_X + m_X) [m_{\Lambda_b} (m_{\Lambda_b} - m_X) f_0]^2}{4 E_X m_{\Lambda_b}^2} + (\text{excited-state contributions}). \quad (51)$$

Sample numerical results for \mathcal{R}_+^V , \mathcal{R}_\perp^V , and \mathcal{R}_0^V are shown in Fig. 3. We further define the quantities

$$R_{f_+}(|\mathbf{p}'|, t) = \frac{2 q^2}{(E_X - m_X)(m_{\Lambda_b} + m_X)} \sqrt{\frac{E_X}{E_X + m_X} \mathcal{R}_+^V(|\mathbf{p}'|, t, t/2)}, \quad (52)$$

$$R_{f_\perp}(|\mathbf{p}'|, t) = \frac{1}{E_X - m_X} \sqrt{\frac{E_X}{E_X + m_X} \mathcal{R}_\perp^V(|\mathbf{p}'|, t, t/2)}, \quad (53)$$

$$R_{f_0}(|\mathbf{p}'|, t) = \frac{2}{m_{\Lambda_b} - m_X} \sqrt{\frac{E_X}{E_X + m_X} \mathcal{R}_0^V(|\mathbf{p}'|, t, t/2)}, \quad (54)$$

where we evaluate the ratios \mathcal{R} at $t' = t/2$ to minimize excited-state contamination at a given value of the source-sink separation t (if t/a is odd, we average \mathcal{R} over $t' = (t+a)/2$ and $t' = (t-a)/2$ instead). The notation with the absolute value indicates that we average over the directions of \mathbf{p}' . Equations (52-54) yield

$$R_{f_+}(|\mathbf{p}'|, t) = f_+ + (\text{excited-state contributions}), \quad (55)$$

$$R_{f_\perp}(|\mathbf{p}'|, t) = f_\perp + (\text{excited-state contributions}), \quad (56)$$

$$R_{f_0}(|\mathbf{p}'|, t) = f_0 + (\text{excited-state contributions}), \quad (57)$$

where the excited-state contributions decay exponentially with t . We checked that the helicity form factors (plus the corresponding excited-state contributions, for the separations we utilize) are all positive by analyzing individual three-point functions, so that the square roots in Eqs. (52-54) give the correct signs. Although not explicitly annotated, the form factors in all of the above expressions depend on $|\mathbf{p}'|$ and on the lattice parameters. For the axial-vector current, we define $\mathcal{R}_{+, \perp, 0}^A$ as in Eq. (46-48) but with $\Gamma = \gamma^\mu \gamma_5$ in the three-point functions. The axial-vector helicity form factors are then extracted as

$$R_{g_+}(|\mathbf{p}'|, t) = \frac{2 q^2}{(E_X + m_X)(m_{\Lambda_b} - m_X)} \sqrt{\frac{E_X}{E_X - m_X} \mathcal{R}_+^A(|\mathbf{p}'|, t, t/2)}, \quad (58)$$

$$R_{g_\perp}(|\mathbf{p}'|, t) = \frac{1}{E_X + m_X} \sqrt{-\frac{E_X}{E_X - m_X} \mathcal{R}_\perp^A(|\mathbf{p}'|, t, t/2)}, \quad (59)$$

$$R_{g_0}(|\mathbf{p}'|, t) = \frac{2}{m_{\Lambda_b} + m_X} \sqrt{\frac{E_X}{E_X - m_X} \mathcal{R}_0^A(|\mathbf{p}'|, t, t/2)}. \quad (60)$$

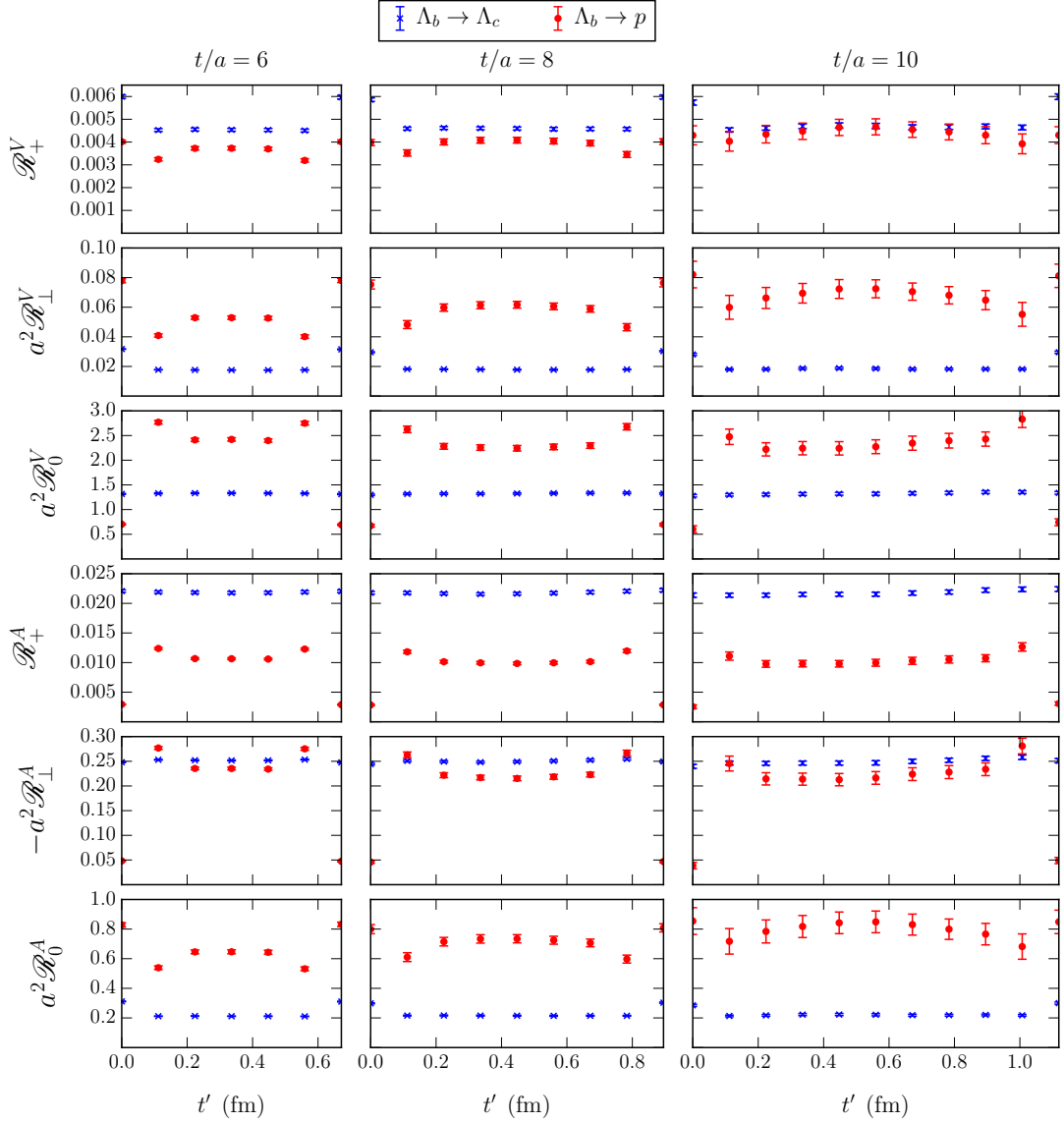


FIG. 3. Numerical results for the vector-current ratios (46), (47), (48) and their axial-vector counterparts, at $|\mathbf{p}'|^2 = 3(2\pi/L)^2$, plotted for three different source-sink separations t . The data shown here are from the C24 data set.

When evaluating the ratios, we take the baryon masses in lattice units, am_{Λ_b} , am_{Λ_c} , and am_N , from exponential fits to the zero-momentum two-point functions for each data set; see Table VI. We then compute the energies $aE_{\Lambda_c}(\mathbf{p}')$, and $aE_N(\mathbf{p}')$ from these masses using the relativistic continuum dispersion relation, and we also compute a^2q^2 from these masses and energies. Because the form factors are dimensionless, the values of the lattice spacing are not needed at this stage. The ratios are evaluated using statistical bootstrap, and we use corresponding bootstrap samples for the masses to take into account all correlations.

As mentioned earlier, except in the case of the C14 data set, we have “full- $\mathcal{O}(a)$ improvement” (“FI”) data only for three source-sink separations in each data set, but we have data with “partial $\mathcal{O}(a)$ -improvement” (“PI”) for all source-sink separations in the ranges shown in Table V. To account for this, we computed the ratios

$$\frac{R_f^{(\text{FI})}(|\mathbf{p}'|, t)}{R_f^{(\text{PI})}(|\mathbf{p}'|, t)}, \quad (61)$$

where $f = f_+, f_\perp, f_0, g_+, g_\perp, g_0$, for those source-sink separations where both $R_f^{(\text{FI})}$ and $R_f^{(\text{PI})}$ are available. Numerical results for Eq. (61) from the C14 data set (where we have FI data for all values of t) are shown in Fig. 4. In the case

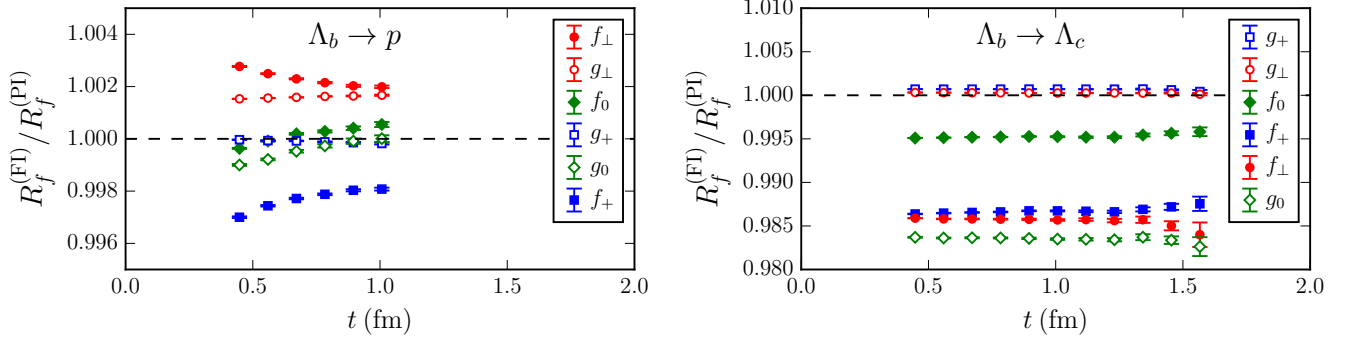


FIG. 4. Ratios of the “fully $\mathcal{O}(a)$ -improved” (“FI”) and “partially $\mathcal{O}(a)$ -improved” (“PI”) data for $R_f(t)$ for the six different helicity form factors, at $|\mathbf{p}'|^2 = 3(2\pi/L)^2$, from the C14 data set. The partially improved data only include the currents $\bar{q}\Gamma\gamma_j\vec{\nabla}_j b$ for the $\mathcal{O}(a)$ -improvement, where $\bar{q} = \bar{u}, \bar{c}$. For $\Lambda_b \rightarrow p$, these are the only currents needed at tree level and the ratio is very close to 1. For $\Lambda_b \rightarrow \Lambda_c$, the ratio deviates from 1 significantly more, because the currents $\bar{c}\vec{\nabla}_j\gamma_j\Gamma b$ are missing the partially improved data, but are needed already at tree level in this case. The range of source-sink separations shown for $\Lambda_b \rightarrow p$ is smaller because the statistical fluctuations in the correlators were too large to reliably compute the individual quantities $R_f(t)$ for $t > 1.0$ fm in this case.

of $\Lambda_b \rightarrow \Lambda_c$ (Fig. 4 right), the correction is as large as 2% for some of the form factors, but is independent of the source-sink separation to a high degree (even though $R_f^{(FI)}$ and $R_f^{(PI)}$ individually have a strong t -dependence). The same behavior is found at other values of the momentum. In the case of $\Lambda_b \rightarrow p$ (Fig. 4 left), the correction shows a more significant dependence on the source-sink separation, but is smaller than 0.3% for all form factors. For the data sets other than C14 we therefore performed constant fits to the ratios (61) as a function of t , individually for each form factor f , each momentum $|\mathbf{p}'|$, and each data set. If these fits had a poor χ^2/dof , we excluded the shortest or the two shortest separations. In this way, we obtained correction factors, which we then applied to $R_f^{(PI)}(|\mathbf{p}'|, t)$ at all separations, to effectively obtain $R_f^{(FI)}(|\mathbf{p}'|, t)$ at all separations. This procedure is accurate to better than permille level. In the following, all ratios $R_f(|\mathbf{p}'|, t)$ are understood to be corrected using this procedure for all source-sink separations.

For the further data analysis, we then also formed the linear combinations

$$R_{f_1^V} = \frac{(m_{\Lambda_b} + m_X)^2 R_{f_+} - q^2 R_{f_\perp}}{s_+}, \quad (62)$$

$$R_{f_2^V} = \frac{m_{\Lambda_b}(m_{\Lambda_b} + m_X)(R_{f_\perp} - R_{f_+})}{s_+}, \quad (63)$$

$$R_{f_3^V} = \frac{m_{\Lambda_b}(m_{\Lambda_b} - m_X) [(m_{\Lambda_b} + m_X)^2 (R_{f_0} - R_{f_+}) + q^2 (R_{f_\perp} - R_{f_0})]}{q^2 s_+}, \quad (64)$$

$$R_{f_1^A} = \frac{(m_{\Lambda_b} - m_X)^2 R_{g_+} - q^2 R_{g_\perp}}{s_-}, \quad (65)$$

$$R_{f_2^A} = \frac{m_{\Lambda_b}(m_{\Lambda_b} - m_X)(R_{g_+} - R_{g_\perp})}{s_-}, \quad (66)$$

$$R_{f_3^A} = \frac{m_{\Lambda_b}(m_{\Lambda_b} + m_X) [(m_{\Lambda_b} - m_X)^2 (R_{g_+} - R_{g_0}) + q^2 (R_{g_0} - R_{g_\perp})]}{q^2 s_-}, \quad (67)$$

which, according to the relations in Eqs. (8)-(13), become equal to the Weinberg form factors at large t . To extract the ground-state form factors from $R_f(|\mathbf{p}'|, t)$ (for both the helicity and Weinberg form factors), we performed correlated fits of the t -dependence including exponential correction terms to account for the leading excited-state contributions, thereby extrapolating $R_f(|\mathbf{p}'|, t)$ to $t = \infty$. To discuss these extrapolations in more detail, it is convenient to denote the data for $R_f(|\mathbf{p}'|, t)$ by

$$R_{f,i,n}(t), \quad (68)$$

where $f = f_+, f_\perp, f_0, g_+, g_\perp, g_0, f_1^V, f_2^V, f_3^V, f_1^A, f_2^A, f_3^A$ labels the form factors, $i = \text{C14, C24, C54, F23, F43, F63}$ labels the data set (cf. Table I), and n labels the final-state momentum via $|\mathbf{p}'|^2 = n(2\pi)^2/L^2$. We performed the fits using

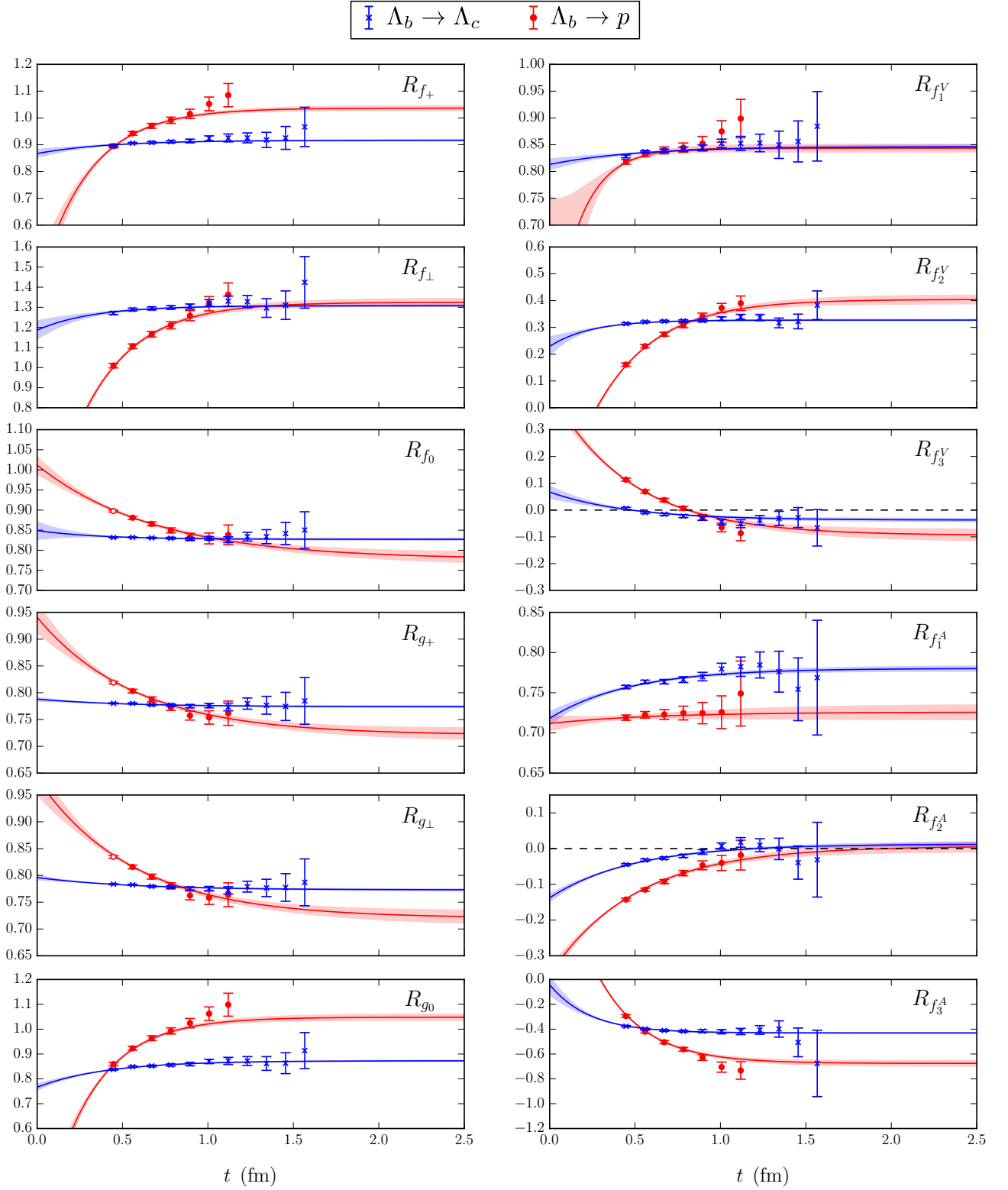


FIG. 5. Extrapolations of $R_f(|\mathbf{p}'|, t)$ to infinite source-sink separation. The data shown here are at momentum $|\mathbf{p}'|^2 = 3(2\pi/L)^2$, and are from the C24 data set. For each momentum, all vector (or axial vector) form factors from all data sets are fitted simultaneously as explained in the main text.

the functions

$$R_{f,i,n}(t) = f_{i,n} + A_{f,i,n} e^{-\delta_{f,i,n} t}, \quad \delta_{f,i,n} = \delta_{\min} + e^{l_{f,i,n}} \text{ GeV}, \quad (69)$$

with parameters $f_{i,n}$, $A_{f,i,n}$, and $l_{f,i,n}$, where $f_{i,n}$ are the form factors we aim to extract. By writing the energy-gaps $\delta_{f,i,n}$ in the above form, we impose the constraint $\delta_{f,i,n} > \delta_{\min}$. We chose $\delta_{\min} = 170$ MeV, which is smaller than any expected energy gap (given our prior knowledge of the hadron spectrum at our values of the pion masses). This constraint has negligible effect in most cases, but prevents numerical instabilities for some form factors at certain momenta where the data show no discernible excited-state contamination.

At each momentum n , we perform one coupled fit to all the data for the vector-current form factors (f_+ , f_\perp , f_0 , f_1^V , f_2^V , f_3^V) and another coupled fit to all the data for the axial-vector-current form factors (g_+ , g_\perp , g_0 , f_1^A , f_2^A , f_3^A). This allows us to implement two additional constraints to stabilize the fits, based on the following knowledge:

- Because the lattice size, L (in physical units), is equal within uncertainties for all data sets ($L \approx 2.7$ fm), the squared momentum $|\mathbf{p}'|^2 = n(2\pi/L)^2$ for a given n is also equal within uncertainties for all data sets. This means that the energy levels, and hence the parameters $l_{f,i,n}$, are expected to be approximately equal across all data sets i , up to some dependence on the pion mass and the lattice spacing.
- By construction, the data $R_{f,i,n}(t)$ for the helicity and Weinberg form factors exactly satisfy the defining relations (62)-(62) at each value of the source-sink separation. The extracted ground-state form factors $f_{i,n}$ should also satisfy these relations.

For the coupled fit to all vector form factor data at a given momentum n , we therefore add the following terms, corresponding to Gaussian priors, to the χ^2 function:

$$\begin{aligned} \chi_{V,n}^2 \rightarrow \chi_{V,n}^2 + \sum_f & \left[\frac{(l_{f,C14,n} - l_{f,C24,n})^2}{[\sigma_m^{C14,C24}]^2} + \frac{(l_{f,C24,n} - l_{f,C54,n})^2}{[\sigma_m^{C24,C54}]^2} + \frac{(l_{f,F23,n} - l_{f,F43,n})^2}{[\sigma_m^{F23,F43}]^2} \right. \\ & \left. + \frac{(l_{f,F43,n} - l_{f,F63,n})^2}{[\sigma_m^{F43,F63}]^2} + \frac{(l_{f,C54,n} - l_{f,F63,n})^2}{[\sigma_m^{C54,F63}]^2} + \sigma_a^2 \right] \\ & + \sum_i \left(f_{+,i,n} - f_{1,i,n}^V - \frac{q_{i,n}^2}{m_{\Lambda_b,i}(m_{\Lambda_b,i} + m_{X,i})} f_{2,i,n}^V \right)^2 / \sigma_f^2 \\ & + \sum_i \left(f_{\perp,i,n} - f_{1,i,n}^V - \frac{m_{\Lambda_b,i} + m_{X,i}}{m_{\Lambda_b,i}} f_{2,i,n}^V \right)^2 / \sigma_f^2 \\ & + \sum_i \left(f_{0,i,n} - f_{1,i,n}^V - \frac{q_{i,n}^2}{m_{\Lambda_b,i}(m_{\Lambda_b,i} - m_{X,i})} f_{3,i,n}^V \right)^2 / \sigma_f^2, \end{aligned} \quad (70)$$

where $\sigma_a = 0.1$ and

$$[\sigma_m^{i,j}]^2 = w_m^2 [(m_\pi^i)^2 - (m_\pi^j)^2]^2, \quad (71)$$

with $w_m = 4 \text{ GeV}^{-2}$. With these widths, the first two lines in Eq. (70) implement the constraint that the energy gaps ($\delta_{f,i,n} - \delta_{\min}$) at given momentum n should not change by more than 10% when going from the fine to the coarse lattice spacing and not more than 400% times the change in m_π^2 (in GeV^2); both are reasonable assumptions given the prior experience with hadron spectroscopy in lattice QCD. Note that absolute variations of $l_{f,i,n}$ translate to relative variations of $(\delta_{f,i,n} - \delta_{\min})$ because $d[\exp(l_{f,i,n})]/\exp(l_{f,i,n}) = dl_{f,i,n}$. The last three lines in Eq. (70) enforce the relations (62)-(64) between the ground-state vector form factors in the helicity and Weinberg definitions (we set $\sigma_f = 10^{-4}$). For the fit to the axial vector form factor data, analogous terms are added to $\chi_{A,n}^2$.

We initially included all available values of t in the fits, and then removed data points for each form factor at the smallest t until the fits had good quality as determined by the correlated χ^2/dof . To estimate the remaining systematic uncertainties associated with higher excited states, we then further removed the next-lowest values of t simultaneously for all $R_{f,i,n}$ and computed the resulting shifts in $f_{i,n}$. We then took the larger of the following two as our estimate of the excited-state systematic uncertainty: i) the shift in $f_{i,n}$ at the given momentum n , and ii) the average of the shifts $f_{i,n}$ over all momenta n . We added these excited-state uncertainties in quadrature to the statistical uncertainties in $f_{i,n}$. All result for $f_{i,n}$ are listed in Appendix A. As can be seen in Tables XIV and XVI, the results for the second-class form factor f_2^A are very close to or consistent with zero for both $\Lambda_b \rightarrow \Lambda_c$ and $\Lambda_b \rightarrow \Lambda_c$, despite the rather large mass differences $m_b - m_u$ and $m_b - m_c$. The results for the other second-class form factor f_3^A are significantly nonzero, but are still noticeably smaller than the results for the first-class form factors.

V. CHIRAL/CONTINUUM/KINEMATIC EXTRAPOLATION OF THE FORM FACTORS

The last step in the data analysis is to perform fits of form factor results $\{f_{i,n}\}$ using suitable functions describing the dependence on the momentum transfer, the dependence on the up and down quark masses (or equivalently the pion mass), and the dependence on the lattice spacing. We perform global fits of the helicity form factors based on the simplified z -expansion [37], modified to account for pion-mass and lattice-spacing dependence. The expansion parameter z^f for a form factor f is defined as

$$z^f(q^2) = \frac{\sqrt{t_+^f - q^2} - \sqrt{t_+^f - t_0}}{\sqrt{t_+^f - q^2} + \sqrt{t_+^f - t_0}}, \quad (72)$$

where we choose

$$t_0 = (m_{\Lambda_b} - m_X)^2, \quad (73)$$

so that the point $z = 0$ corresponds to $q^2 = q_{\max}^2$ (i.e. $\mathbf{p}' = 0$ in the Λ_b rest frame). The values of t_+^f are discussed further below. After factoring out the leading pole contribution, we expand the form factors in a power series in z^f . We find that our lattice data can be described well by keeping only the zeroth and first order in z^f . As explained further below, we also perform higher-order fits to estimate systematic uncertainties. Our nominal (as opposed to higher-order) fits are of the form

$$f(q^2) = \frac{1}{1 - q^2/(m_{\text{pole}}^f)^2} \left[a_0^f \left(1 + c_0^f \frac{m_\pi^2 - m_{\pi,\text{phys}}^2}{\Lambda_\chi^2} \right) + a_1^f z^f(q^2) \right] \\ \times \left[1 + b^f \frac{|\mathbf{p}'|^2}{(\pi/a)^2} + d^f \frac{\Lambda_{\text{QCD}}^2}{(\pi/a)^2} \right], \quad (74)$$

with fit parameters a_0^f , a_1^f , c_0^f , b^f , and d^f . Here, m_π are the valence pion masses of each data set (see Table I), and $m_{\pi,\text{phys}} = 134.8 \text{ MeV}$ is the physical pion mass in the isospin limit [63]. As discussed in Ref. [29], chiral-perturbation-theory predictions for the pion-mass dependence of the form factors considered here are unavailable and would be of limited use because of the large momentum scales in these matrix elements, and because of the large number of low-energy constants. In Eq. (74) we describe the pion-mass dependence through the factor $1 + c_0^f(m_\pi^2 - m_{\pi,\text{phys}}^2)/\Lambda_\chi^2$ multiplying a_0 . Here, we introduced the scale $\Lambda_\chi = 4\pi f$ with $f = 132 \text{ MeV}$ so that c_0 becomes dimensionless. Because our lattice actions and currents are $\mathcal{O}(a)$ -improved, we allow for a quadratic dependence on the lattice spacing via the factor in the second line of Eq. (74), where $\Lambda_{\text{QCD}} = 0.5 \text{ GeV}$. The parameters b^f and d^f describe the momentum-dependent and momentum-independent parts of the lattice discretization errors. We use the individual lattice QCD results for the baryon masses from each dataset (see Table VI) to evaluate $a^2 q^2$ and z , and we take into account the uncertainties and correlations of these masses. We set the pole masses equal to

$$am_{\text{pole}}^f = am_{\text{PS}} + a\Delta^f, \quad (75)$$

where am_{PS} is the pseudoscalar B_u or B_c mass (in lattice units) computed individually for each data set (and also listed in Table VI), and Δ^f is the mass splitting (in GeV) between the meson with the relevant quantum numbers and the pseudoscalar B_u (for $\Lambda_b \rightarrow p$) or B_c (for $\Lambda_b \rightarrow \Lambda_c$). We use fixed values of Δ^f for all data sets, based on experimental data (where available) [1] and averages of our lattice QCD results over the different data sets. These values are given in Table VII. The pole factor is then written as

$$\frac{1}{1 - (a^2 q^2)/(am_{\text{PS}} + a\Delta^f)^2}, \quad (76)$$

so that the explicit value of the lattice spacing is needed only for the term $a\Delta^f$. Note that when the input values of Δ^f are varied, the shape parameters a_0^f and a_1^f returned from the fit change in such a way as to largely cancel the effect of this variation on the form factors (varying Δ^f by 10% changes the form factors themselves by less than 1%).

The parameter t_+^f should be set equal to or below the location of any singularities remaining after factoring out the leading pole contribution. The $\Lambda_b \rightarrow p$ and $\Lambda_b \rightarrow \Lambda_c$ form factors (in infinite volume) have branch cuts starting at $q^2 = (m_B + m_\pi)^2$ and $q^2 = (m_B + m_D)^2$, respectively. In the case of $\Lambda_b \rightarrow p$, the form factors f_0 , g_+ , g_\perp have no poles below this branch cut, and the form factors f_+ , f_\perp , g_0 only have a single pole below $q^2 = (m_B + m_\pi)^2$, which

f	J^P	$t_+^f(\Lambda_b \rightarrow p)$	$m_{\text{pole}}^f(\Lambda_b \rightarrow p)$	$\Delta^f(\Lambda_b \rightarrow p)$	$t_+^f(\Lambda_b \rightarrow \Lambda_c)$	$m_{\text{pole}}^f(\Lambda_b \rightarrow \Lambda_c)$	$\Delta^f(\Lambda_b \rightarrow \Lambda_c)$
f_+, f_\perp	1^-	$(m_B + m_\pi)^2$	$m_B + \Delta^f$	46 MeV	$(m_{\text{pole}}^f)^2$	$m_{B_c} + \Delta^f$	56 MeV
f_0	0^+	$(m_B + m_\pi)^2$	$m_B + \Delta^f$	377 MeV	$(m_{\text{pole}}^f)^2$	$m_{B_c} + \Delta^f$	449 MeV
g_+, g_\perp	1^+	$(m_B + m_\pi)^2$	$m_B + \Delta^f$	427 MeV	$(m_{\text{pole}}^f)^2$	$m_{B_c} + \Delta^f$	492 MeV
g_0	0^-	$(m_B + m_\pi)^2$	$m_B + \Delta^f$	0	$(m_{\text{pole}}^f)^2$	$m_{B_c} + \Delta^f$	0

TABLE VII. Values of t_+^f and m_{pole}^f . To evaluate the form factors in the physical limit, $m_B = 5.279$ GeV, $m_\pi = 134.8$ MeV, and $m_{B_c} = 6.276$ GeV should be used.

gets removed by the explicit factor of $1/[1 - q^2/(m_{\text{pole}}^f)^2]$. We therefore set $t_+^f = (m_B + m_\pi)^2$ for all $\Lambda_b \rightarrow p$ form factors. More precisely, to evaluate the dimensionless quantity $a^2 t_+^f$ in the fit, we use

$$a^2 t_+^f = (am_{\text{PS}} + am_{\pi, \text{phys}})^2 \quad (\text{for } \Lambda_b \rightarrow p), \quad (77)$$

where am_{PS} is the pseudoscalar B_u mass (in lattice units) computed individually for each data set, and $m_{\pi, \text{phys}} = 134.8$ MeV. This means that the value of the lattice spacing is needed only for the term $am_{\pi, \text{phys}}$. We checked that using the individual lattice pion masses of each data set instead of the physical pion mass has a negligible effect on the extrapolated form factors. In the case of $\Lambda_b \rightarrow \Lambda_c$, the onset of the branch cut, $m_B + m_D$, is several hundred MeV above the lowest pole for all form factors, and there may be additional poles below $m_B + m_D$. We therefore set $t_+^f = (m_{\text{pole}}^f)^2$ for the $\Lambda_b \rightarrow \Lambda_c$ form factors; more precisely,

$$a^2 t_+^f = (am_{\text{PS}} + a\Delta^f)^2 \quad (\text{for } \Lambda_b \rightarrow \Lambda_c), \quad (78)$$

where am_{PS} is the pseudoscalar B_c mass (in lattice units) computed individually for each data set, as discussed above. With this choice of t_+^f , the factors of $1/[1 - q^2/(m_{\text{pole}}^f)^2]$ are not strictly necessary, but we find that they improve the quality of the fit at first order in the z expansion.

We implement the constraint $g_\perp(q_{\text{max}}^2) = g_+(q_{\text{max}}^2)$ [Eq. (16)] at $z^{g_\perp, g_+} = 0$ and $a = 0$ by using shared parameters $a_0^{g_\perp, g_+}$ and $c_0^{g_\perp, g_+}$ for these two form factors. We impose the constraints $f_0(0) = f_+(0)$ and $g_0(0) = g_+(0)$ [Eqs. (14) and (15)] using Gaussian priors with widths equal to $\max[z^{f_0}(0), z^{f_+}(0)]^2$ and $\max[z^{g_0}(0), z^{g_+}(0)]^2$, respectively, to allow for missing higher-order terms in z^f . For $\Lambda_b \rightarrow p$, we performed one global fit to all helicity form factors, taking into account the correlations between different form factors, different momenta, and different data sets. For $\Lambda_b \rightarrow \Lambda_c$, such a global fit showed indications of problems associated with a poorly conditioned data covariance matrix, and we additionally performed fits of the subsets $\{f_+, f_0\}$, $\{f_\perp\}$, $\{g_+, g_\perp, g_0\}$ to reduce the sizes of the data covariance matrices. We then took the central values and covariances of the form factor parameters within each subset from these subset fits, and only used the global fit to estimate the cross-covariances between the parameters in different subsets.

The physical limit is given by $a \rightarrow 0$ and $m_\pi \rightarrow m_{\pi, \text{phys}}$, and correspondingly Eq. (74) reduces to the simple form

$$f(q^2) = \frac{1}{1 - q^2/(m_{\text{pole}}^f)^2} [a_0^f + a_1^f z^f(q^2)], \quad (79)$$

where q^2 should be evaluated using the experimental values of the baryon masses, and m_{pole}^f, t_+^f should be set to the values given in Table VII, with $m_B = 5.279$ GeV, $m_\pi = 134.8$ MeV, $m_{B_c} = 6.276$ GeV. The central values and uncertainties of the parameters $\{a_0^f, a_1^f\}$ from the nominal fit are given in Table VIII, and the correlation matrices are given in Table IX. The parameter *covariances* $\text{cov}(p, q)$ can be obtained from the correlations $\text{corr}(p, q)$ and uncertainties σ_p, σ_q using $\text{cov}(p, q) = \sigma_p \sigma_q \text{corr}(p, q)$; the central values and covariance matrices of the fit parameters are also provided as ancillary files with the arXiv submission of this article. Plots of the lattice data along with the physical-limit fit curves are shown in Figs. 6, 7, 8, and 9.

To estimate the systematic uncertainties caused by our assumptions on the lattice-spacing, quark-mass, and q^2 -dependence, we also perform fits that include additional higher-order terms, employing the form

$$f_{\text{HO}}(q^2) = \frac{1}{1 - q^2/(m_{\text{pole}}^f)^2} \left[a_0^f \left(1 + c_0^f \frac{m_\pi^2 - m_{\pi, \text{phys}}^2}{\Lambda_\chi^2} + \tilde{c}_0^f \frac{m_\pi^3 - m_{\pi, \text{phys}}^3}{\Lambda_\chi^3} \right) + a_1^f \left(1 + c_1^f \frac{m_\pi^2 - m_{\pi, \text{phys}}^2}{\Lambda_\chi^2} \right) z^f(q^2) \right. \\ \left. + a_2^f [z^f(q^2)]^2 \right] \left[1 + b^f \frac{|\mathbf{p}'|^2}{(\pi/a)^2} + d^f \frac{\Lambda_{\text{QCD}}^2}{(\pi/a)^2} + \tilde{b}^f \frac{|\mathbf{p}'|^3}{(\pi/a)^3} + \tilde{d}^f \frac{\Lambda_{\text{QCD}}^3}{(\pi/a)^3} + j^f \frac{|\mathbf{p}'|^2 \Lambda_{\text{QCD}}}{(\pi/a)^3} + k^f \frac{|\mathbf{p}'|^2 \Lambda_{\text{QCD}}^2}{(\pi/a)^3} \right]. \quad (80)$$

Parameter	$\Lambda_b \rightarrow p$	$\Lambda_b \rightarrow \Lambda_c$
a_0^{f+}	0.4382 ± 0.0315	0.8146 ± 0.0167
a_1^{f+}	-0.6452 ± 0.2093	-4.8990 ± 0.5425
a_0^{f0}	0.4189 ± 0.0256	0.7439 ± 0.0125
a_1^{f0}	-0.7862 ± 0.2038	-4.6480 ± 0.6084
$a_0^{f\perp}$	0.5389 ± 0.0435	1.0780 ± 0.0256
$a_1^{f\perp}$	-0.8069 ± 0.3039	-6.4170 ± 0.8480
$a_0^{g\perp, g+}$	0.3912 ± 0.0198	0.6847 ± 0.0086
a_1^{g+}	-0.8167 ± 0.1749	-4.4310 ± 0.3572
a_0^{g0}	0.4526 ± 0.0292	0.7396 ± 0.0143
a_1^{g0}	-0.7817 ± 0.1886	-4.3660 ± 0.3314
$a_1^{g\perp}$	-0.9061 ± 0.1956	-4.4630 ± 0.3613

TABLE VIII. Central values and uncertainties of the nominal form factor parameters for $\Lambda_b \rightarrow p$ and $\Lambda_b \rightarrow \Lambda_c$. See Table IX for the correlation matrices.

This allows for higher-order variation in the lattice spacing, quark masses, and momentum dependence. The data themselves do not determine this more complex form sufficiently well, so we constrain the higher-order coefficients $\tilde{c}_0^f, c_1^f, \tilde{b}^f, \tilde{d}^f, j^f, k^f$ to be natural-sized using Gaussian priors with central value 0 and width 10. We constrain the second-order z -expansion coefficients a_2^f using Gaussian priors with central values 0 and widths given by approximately twice the magnitude of the previous (nominal) fit results for a_1^f . Given that this fit is quadratic in z^f , we now impose the kinematic constraints (14) and (15) at $q^2 = 0$ up to widths of $\max[z^{f0}(0), z^{f+}(0)]^3$ and $\max[z^{g0}(0), z^{g+}(0)]^3$, respectively.

In the higher-order fit, we use bootstrap data for the correlator ratios in which the matching- and $\mathcal{O}(a)$ -improvement coefficients were drawn from Gaussian random distributions with central values and widths according to Table III. Thus, the higher-order fit results also include the perturbation-theory systematic uncertainty. To take into account the uncertainties of the lattice spacings, we promote the lattice spacings of the different ensembles to fit parameters, constrained with Gaussian priors according to the central values and uncertainties given in Table I. The systematic uncertainties caused by the finite lattice volume cannot easily be estimated from the data, because all of our data sets have approximately the same lattice size, $L \approx 2.7$ fm. Finite-volume effects have been calculated using chiral perturbation theory for the nucleon magnetic moment [64] and axial charge [65], and, specifically for the ensembles used herein, for the heavy-baryon axial couplings [61, 66]. Based on this experience, we estimate that the finite-volume systematic uncertainties in our results are 3% for the $\Lambda_b \rightarrow p$ form factors, and 1.5% for the $\Lambda_b \rightarrow \Lambda_c$ form factors. The neglected isospin breaking effects in the form factors are estimated to be of order $\mathcal{O}((m_d - m_u)/\Lambda_{\text{QCD}}) \approx 0.5\%$ and $\mathcal{O}(\alpha_{\text{e.m.}}) \approx 0.7\%$. Finally, there is an uncertainty resulting from the tuning of the relativistic heavy quark (RHQ) parameters, which was performed in Ref. [51] for the b quark and in Ref. [52] for the c quark. In Ref. [12], the same b -quark parameters were used to compute the $B \rightarrow \pi$ form factors on the same gauge field configurations as in the present work, and the uncertainties of $am_Q^{(b)}$, $\xi^{(b)}$, and $c_{E,B}^{(b)}$ were propagated to the form factors by repeating the calculation for multiple values of $am_Q^{(b)}$, $\xi^{(b)}$, and $c_{E,B}^{(b)}$. The resulting uncertainties in the $B \rightarrow \pi$ form factors were found to be 1%. We could not afford to repeat the present calculation for multiple values of the RHQ parameters, and therefore adopt the 1% estimate also for the b -quark parameter uncertainty in the $\Lambda_b \rightarrow p$ and $\Lambda_b \rightarrow \Lambda_c$ form factors. We are unable to estimate the c -quark parameter uncertainty in the $\Lambda_b \rightarrow \Lambda_c$ form factors at this time, but we note that our choice of parameters precisely reproduces the experimental values of the charmonium masses and hyperfine splittings, as well as the relativistic continuum dispersion relation, on both the coarse and the fine lattices [52]. To estimate the effect of the light-quark-mass uncertainties, we promote the pion masses (in lattice units) to fit parameters, constrained with Gaussian priors according to the central values and widths given in Ref. [36]. We find that this results in a smaller than 0.1% uncertainty in the $\Lambda_b \rightarrow p$ and $\Lambda_b \rightarrow \Lambda_c$ form factors. To incorporate the finite-volume, isospin breaking, and RHQ parameter tuning uncertainties in the higher-order fit, we add these uncertainties to the data covariance matrix before performing the fit. We assume that these uncertainties are 100% correlated between the different data sets and different final-state momenta, and between the three different form factors corresponding to the same type of current (vector or axial vector).

In the physical limit, the higher-order fit functions reduce to

$$f_{\text{HO}}(q^2) = \frac{1}{1 - q^2/(m_{\text{pole}}^f)^2} [a_0^f + a_1^f z^f(q^2) + a_2^f [z^f(q^2)]^2]. \quad (81)$$

The values of the parameters a_0^f, a_1^f, a_2^f , their total uncertainties, and their correlation matrices are given in Tables X and XI, and are also included as ancillary files with the arXiv submission. The recommended procedure for computing the central value, statistical uncertainty, and total systematic uncertainty of a general observable depending on the form factor parameters (for example, a differential decay rate at a particular value of q^2 , or an integrated decay rate, or a ratio of decay rates) is the following:

1. Compute the observable and its uncertainty using the nominal form factors given by Eq. (79), with the parameter values and correlation matrices from Tables VIII and IX. Denote the so-obtained central value and uncertainty as

$$O, \sigma_O. \quad (82)$$

2. Compute the same observable and its uncertainty using the higher-order form factors given by Eq. (81), with the parameter values and correlation matrices from Tables X and XI. Denote the so-obtained central value and uncertainty as

$$O_{\text{HO}}, \sigma_{O,\text{HO}}. \quad (83)$$

3. The final result for the observable is then given by

$$O \pm \underbrace{\sigma_O}_{\text{stat.}} \pm \underbrace{\max(|O_{\text{HO}} - O|, \sqrt{|\sigma_{O,\text{HO}}^2 - \sigma_O^2|})}_{\text{syst.}}. \quad (84)$$

In other words, the central value and statistical uncertainty are obtained from the nominal fit, and the systematic uncertainty is given by the larger of the following two quantities: i) the shift in the central value between the nominal fit and the higher-order fit, and ii) the increase in the uncertainty (computed in quadrature as shown above) from the nominal fit to the higher-order fit. The statistical and systematic uncertainties in Eq. (84) should be added in quadrature. By construction, the above procedure gives the combined systematic uncertainty associated with the continuum extrapolation, chiral extrapolation, z expansion, perturbative matching, scale setting, b -quark parameter tuning, finite volume, and missing isospin symmetry breaking/QED.

Plots of the form factors including the systematic uncertainties, computed as explained above, are shown in Figs. 10 and 12. The relative systematic uncertainties in the form factors are shown in Figs. 11 and 13. In addition to the combined systematic uncertainty (thick black curves), these figures also show the individual sources of uncertainty. The individual systematic uncertainties were estimated using additional fits as follows:

- Continuum extrapolation uncertainty: only the higher-order terms with coefficients $\tilde{b}^f, \tilde{d}^f, j^f, k^f$ were added to Eq. (74).
- Chiral extrapolation uncertainty: only the higher-order terms with coefficients \tilde{c}_0^f, c_1^f were added to Eq. (74).
- z expansion uncertainty: only the higher-order term $a_2^f [z^f(q^2)]^2$ was added to Eq. (74).
- Matching & improvement uncertainty: no higher-order terms were added to Eq. (74), but the the matching- and $\mathcal{O}(a)$ -improvement coefficients were drawn from Gaussian random distributions with central values and widths according to Table III when computing the correlator ratios using bootstrap.
- Scale setting (i.e., lattice spacing) uncertainty: no higher-order terms were added to Eq. (74), but the lattice spacings were promoted to fit parameters constrained with Gaussian priors according to the central values and uncertainties given in Table I.
- Finite-volume effects, missing isospin breaking/QED, and RHQ parameter tuning uncertainties: no higher-order terms were added to Eq. (74), but the estimates of these uncertainties (as discussed above) were added to the data covariance matrix used in the fit.

Figures 11 and 13 show that near $q^2 = q_{\text{max}}^2$, the finite-volume and chiral-extrapolation uncertainties are the largest, but as the momentum $|\mathbf{p}'|$ increases (corresponding to decreasing q^2), the z -expansion and continuum extrapolation uncertainties grow and become dominant. The continuum extrapolation uncertainty should not be interpreted as the actual size of lattice discretization errors; the reason for the large continuum extrapolation uncertainty is primarily that we have only two lattice spacings and our data do not tightly constrain all of the extrapolation coefficients.

Discretization errors associated with the relativistic heavy quark actions used for the b and c quarks are not necessarily well approximated by the leading terms in an expansion in $a\Lambda_{\text{QCD}}$ and $a\mathbf{p}'$. These errors can be described

by mismatches of the coefficients of higher-dimensional operators in the heavy-quark expansions of the lattice theory and continuum QCD [47, 67–69]. In Ref. [12], the resulting heavy-quark discretization errors in the $B \rightarrow \pi$ form factors were estimated using power counting to be of order 2% for the same lattice actions and parameters as used in the present work. For most of the kinematic range, our estimate of the total continuum-extrapolation uncertainty in the $\Lambda_b \rightarrow p$ form factors is larger than this power-counting estimate, see Fig. 11. Similarly, a comparison with the analysis of $B \rightarrow D$ form factors in Ref. [59] suggests that heavy-quark discretization errors in the $\Lambda_b \rightarrow \Lambda_c$ form factors are smaller than or compatible with our estimates of the total continuum-extrapolation uncertainties in the entire kinematic range.

$\Lambda_b \rightarrow p$	a_0^{f+}	a_1^{f+}	$a_0^{f_0}$	$a_1^{f_0}$	$a_0^{f_\perp}$	$a_1^{f_\perp}$	$a_0^{g_\perp, g+}$	a_1^{g+}	$a_0^{g_0}$	$a_1^{g_0}$	$a_1^{g_\perp}$
a_0^{f+}	1	-0.9058	0.5081	-0.4403	0.5299	-0.3987	0.5362	-0.4112	0.6302	-0.5305	-0.3898
a_1^{f+}	-0.9058	1	-0.4280	0.4312	-0.4238	0.3739	-0.4402	0.3912	-0.4901	0.4839	0.3668
$a_0^{f_0}$	0.5081	-0.4280	1	-0.8533	0.4251	-0.3226	0.6963	-0.5274	0.5504	-0.4694	-0.4886
$a_1^{f_0}$	-0.4403	0.4312	-0.8533	1	-0.3525	0.3008	-0.5963	0.5917	-0.4661	0.4554	0.5667
$a_0^{f_\perp}$	0.5299	-0.4238	0.4251	-0.3525	1	-0.8930	0.4748	-0.3554	0.5975	-0.5111	-0.3348
$a_1^{f_\perp}$	-0.3987	0.3739	-0.3226	0.3008	-0.8930	1	-0.3664	0.3156	-0.4349	0.4542	0.2900
$a_0^{g_\perp, g+}$	0.5362	-0.4402	0.6963	-0.5963	0.4748	-0.3664	1	-0.8434	0.6238	-0.5500	-0.7905
a_1^{g+}	-0.4112	0.3912	-0.5274	0.5917	-0.3554	0.3156	-0.8434	1	-0.4761	0.5011	0.8778
$a_0^{g_0}$	0.6302	-0.4901	0.5504	-0.4661	0.5975	-0.4349	0.6238	-0.4761	1	-0.9039	-0.4497
$a_1^{g_0}$	-0.5305	0.4839	-0.4694	0.4554	-0.5111	0.4542	-0.5500	0.5011	-0.9039	1	0.4632
$a_1^{g_\perp}$	-0.3898	0.3668	-0.4886	0.5667	-0.3348	0.2900	-0.7905	0.8778	-0.4497	0.4632	1
$\Lambda_b \rightarrow \Lambda_c$	a_0^{f+}	a_1^{f+}	$a_0^{f_0}$	$a_1^{f_0}$	$a_0^{f_\perp}$	$a_1^{f_\perp}$	$a_0^{g_\perp, g+}$	a_1^{g+}	$a_0^{g_0}$	$a_1^{g_0}$	$a_1^{g_\perp}$
a_0^{f+}	1	-0.6644	0.6827	-0.4853	0.6218	-0.3906	0.4828	-0.3152	0.5636	-0.4317	-0.3763
a_1^{f+}	-0.6644	1	-0.6515	0.9445	-0.3853	0.5109	-0.3831	0.4915	-0.2979	0.4916	0.4764
$a_0^{f_0}$	0.6827	-0.6515	1	-0.7040	0.4208	-0.3620	0.6174	-0.4822	0.4320	-0.4726	-0.4756
$a_1^{f_0}$	-0.4853	0.9445	-0.7040	1	-0.2738	0.4739	-0.3888	0.5261	-0.2164	0.4779	0.4877
$a_0^{f_\perp}$	0.6218	-0.3853	0.4208	-0.2738	1	-0.6637	0.3933	-0.2369	0.5161	-0.3639	-0.2926
$a_1^{f_\perp}$	-0.3906	0.5109	-0.3620	0.4739	-0.6637	1	-0.2903	0.3509	-0.2443	0.3640	0.3400
$a_0^{g_\perp, g+}$	0.4828	-0.3831	0.6174	-0.3888	0.3933	-0.2903	1	-0.7304	0.6365	-0.6743	-0.7301
a_1^{g+}	-0.3152	0.4915	-0.4822	0.5261	-0.2369	0.3509	-0.7304	1	-0.3829	0.8725	0.9171
$a_0^{g_0}$	0.5636	-0.2979	0.4320	-0.2164	0.5161	-0.2443	0.6365	-0.3829	1	-0.6843	-0.4846
$a_1^{g_0}$	-0.4317	0.4916	-0.4726	0.4779	-0.3639	0.3640	-0.6743	0.8725	-0.6843	1	0.8456
$a_1^{g_\perp}$	-0.3763	0.4764	-0.4756	0.4877	-0.2926	0.3400	-0.7301	0.9171	-0.4846	0.8456	1

TABLE IX. Correlation matrices of the nominal form factor parameters for $\Lambda_b \rightarrow p$ (top) and $\Lambda_b \rightarrow \Lambda_c$ (bottom).

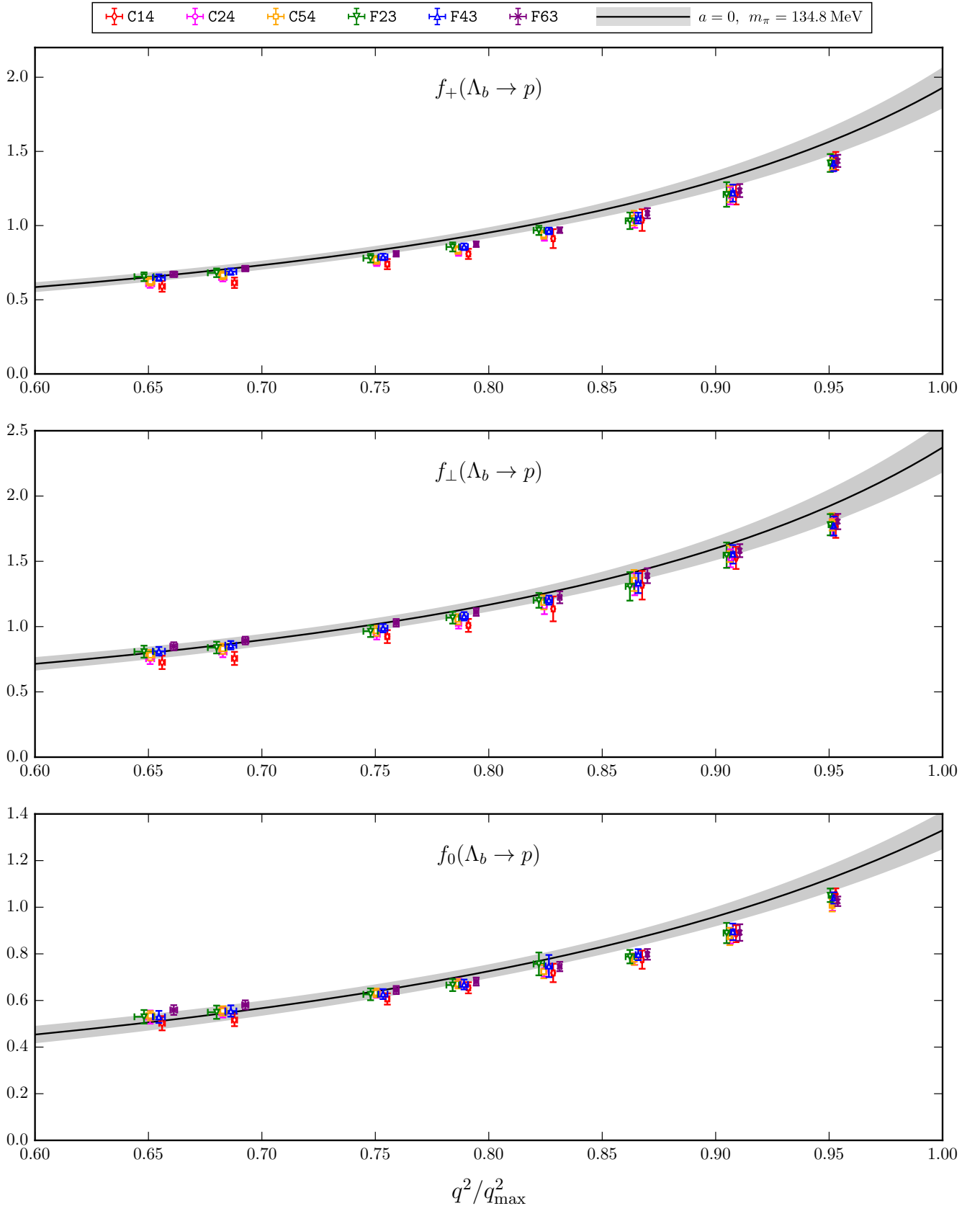


FIG. 6. $\Lambda_b \rightarrow p$ vector form factors: lattice results and extrapolation to the physical limit (nominal fit). The bands indicate the 1σ statistical uncertainty.

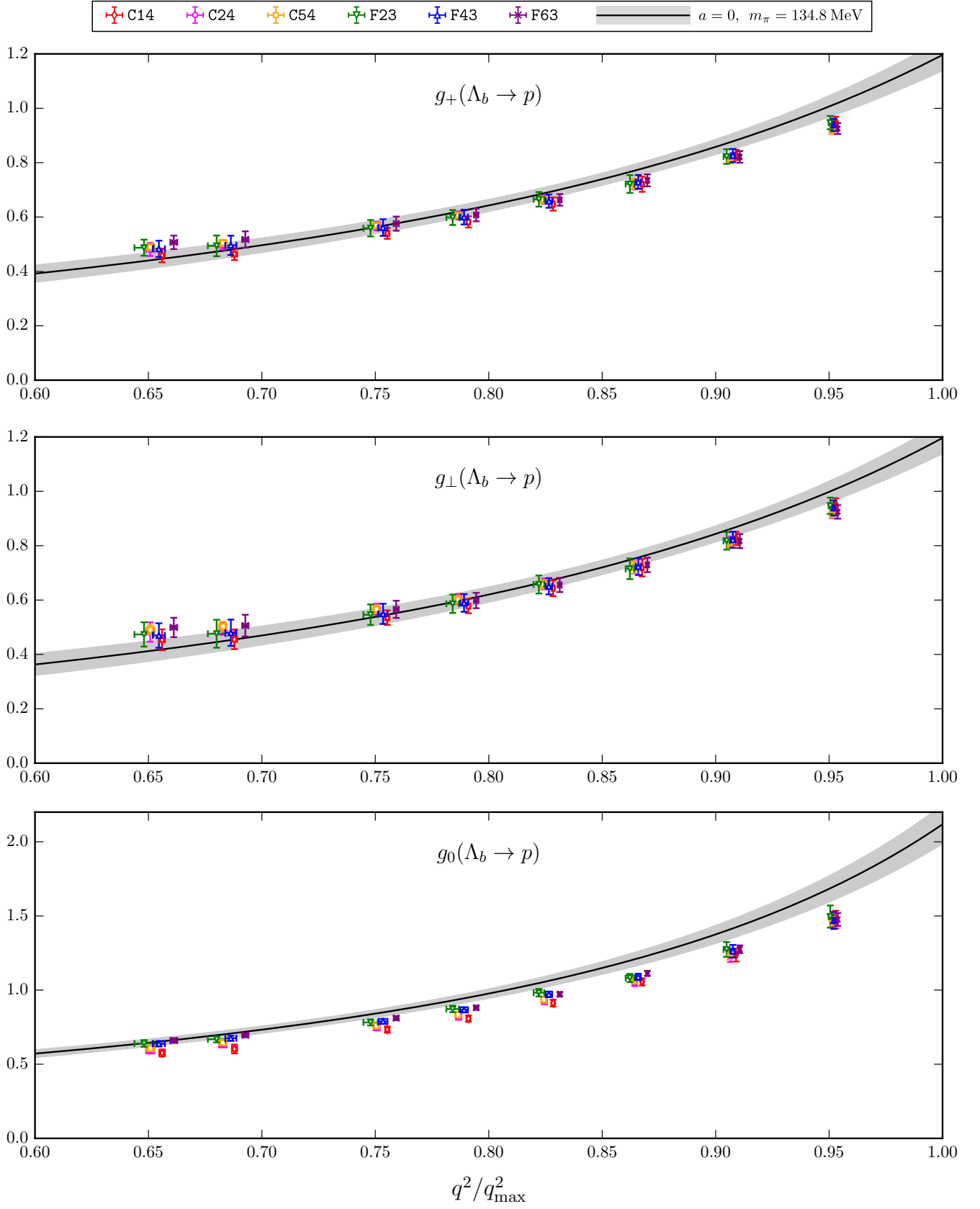


FIG. 7. $\Lambda_b \rightarrow p$ axial-vector form factors: lattice results and extrapolation to the physical limit (nominal fit). The bands indicate the 1σ statistical uncertainty.

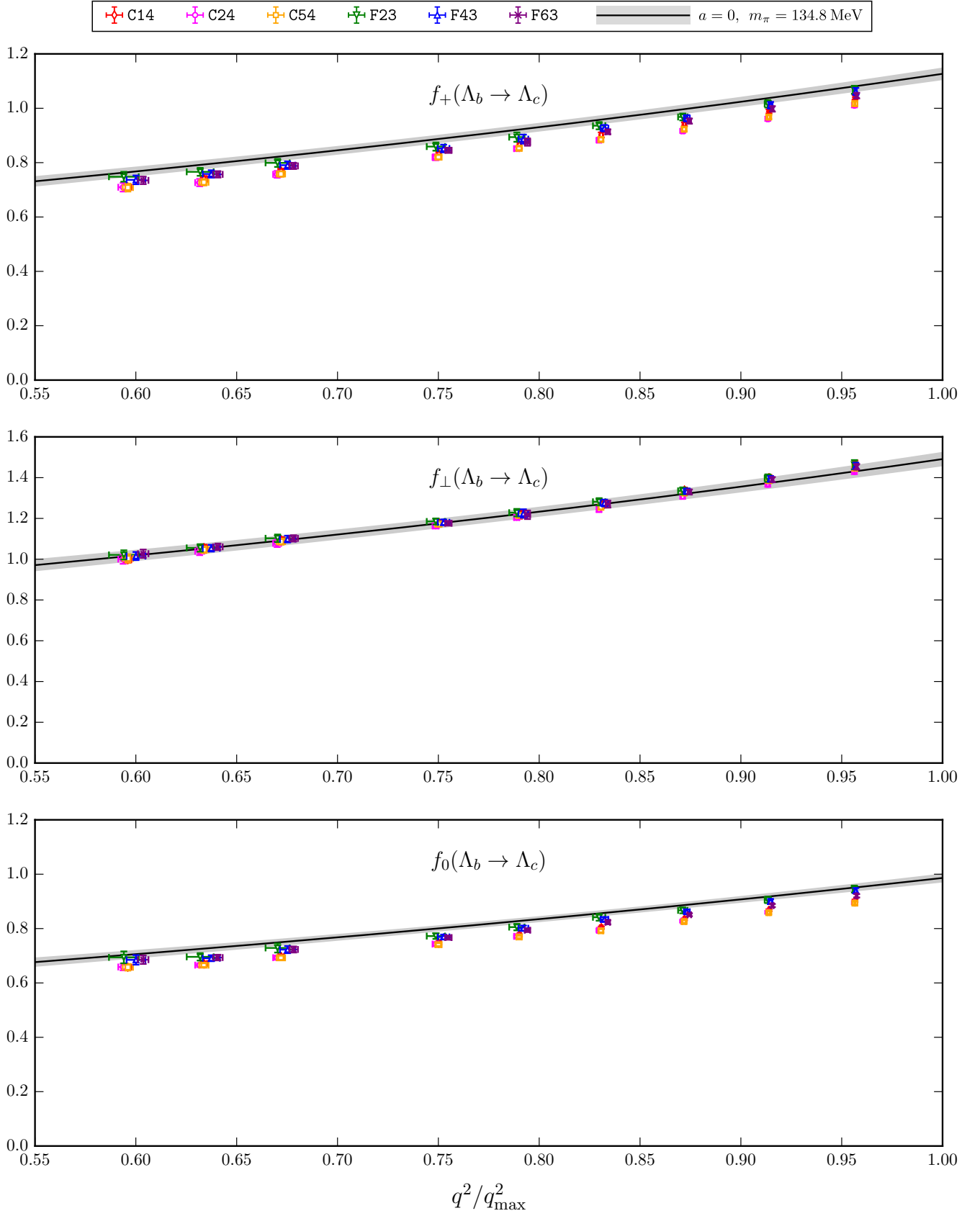


FIG. 8. $\Lambda_b \rightarrow \Lambda_c$ vector form factors: lattice results and extrapolation to the physical limit (nominal fit). The bands indicate the 1σ statistical uncertainty.

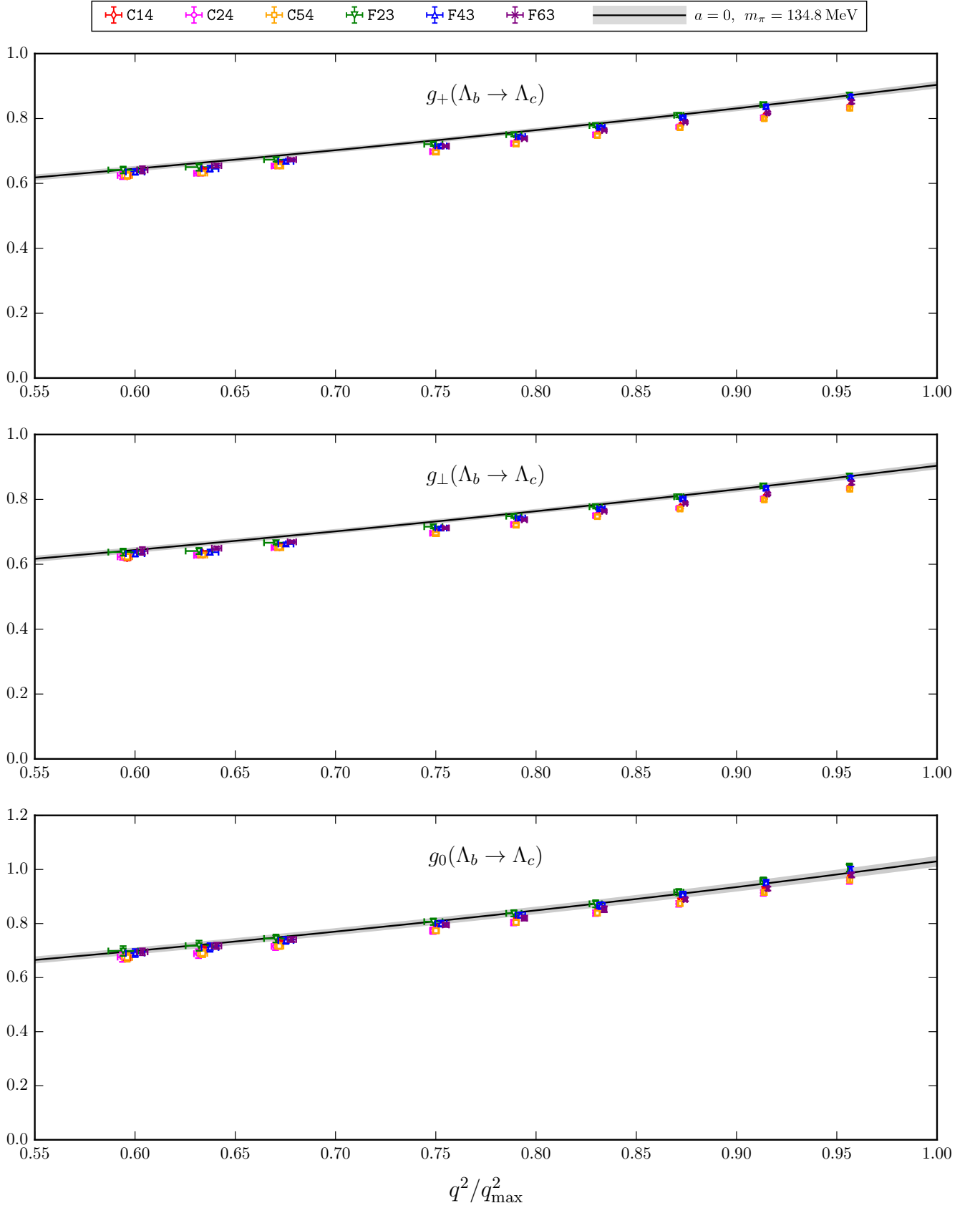


FIG. 9. $\Lambda_b \rightarrow \Lambda_c$ axial-vector form factors: lattice results and extrapolation to the physical limit (nominal fit). The bands indicate the 1σ statistical uncertainty.

Parameter	$\Lambda_b \rightarrow p$	$\Lambda_b \rightarrow \Lambda_c$
$a_0^{f^+}$	0.4251 ± 0.0388	0.8103 ± 0.0276
$a_1^{f^+}$	-0.7088 ± 0.3361	-4.7480 ± 0.9429
$a_2^{f^+}$	0.8925 ± 0.8869	0.7862 ± 8.8020
$a_0^{f^0}$	0.4144 ± 0.0321	0.7389 ± 0.0225
$a_1^{f^0}$	-1.0420 ± 0.3142	-4.5630 ± 0.9426
$a_2^{f^0}$	1.9260 ± 0.9190	2.7050 ± 8.4430
$a_0^{f^\perp}$	0.5214 ± 0.0520	1.0940 ± 0.0435
$a_1^{f^\perp}$	-0.8247 ± 0.4424	-6.4410 ± 1.5010
$a_2^{f^\perp}$	0.7609 ± 1.2770	2.3160 ± 11.320
$a_0^{g^\perp, g^+}$	0.3889 ± 0.0260	0.6848 ± 0.0184
$a_1^{g^+}$	-1.0730 ± 0.2617	-4.3790 ± 0.6954
$a_2^{g^+}$	1.9860 ± 0.8247	1.2810 ± 7.3650
$a_0^{g^0}$	0.4419 ± 0.0388	0.7408 ± 0.0258
$a_1^{g^0}$	-0.8649 ± 0.3481	-4.3860 ± 0.8774
$a_2^{g^0}$	0.9969 ± 0.8955	1.3380 ± 8.0440
$a_1^{g^\perp}$	-1.0840 ± 0.2732	-4.6270 ± 0.7088
$a_2^{g^\perp}$	1.4520 ± 1.0680	1.6140 ± 7.4530

TABLE X. Central values and uncertainties of the higher-order form factor parameters for $\Lambda_b \rightarrow p$ and $\Lambda_b \rightarrow \Lambda_c$. See Table XI for the correlation matrices.

$\Lambda_b \rightarrow p$	$a_0^{f^+}$	$a_1^{f^+}$	$a_2^{f^+}$	$a_0^{f_0}$	$a_1^{f_0}$	$a_2^{f_0}$	$a_0^{f_\perp}$	$a_1^{f_\perp}$	$a_2^{f_\perp}$	$a_0^{g_\perp, g^+}$	$a_1^{g_\perp, g^+}$	$a_2^{g_\perp, g^+}$	$a_0^{g_0}$	$a_1^{g_0}$	$a_2^{g_0}$	$a_0^{g_\perp}$	$a_1^{g_\perp}$	$a_2^{g_\perp}$
$a_0^{f^+}$	1	-0.7671	0.2482	0.5337	-0.2670	-0.0922	0.5121	-0.2469	-0.0180	0.3774	-0.2148	-0.0472	0.4420	-0.2680	0.0018	-0.2284	-0.0231	
$a_1^{f^+}$	-0.7671	1	-0.6611	-0.2486	0.1617	0.0653	-0.2526	0.1671	0.0056	-0.2177	0.1480	0.0287	-0.2496	0.1849	-0.0169	0.1534	0.0147	
$a_2^{f^+}$	0.2482	-0.6611	1	-0.0792	0.0267	0.2795	-0.0035	-0.0120	0.0425	-0.0562	0.0382	0.0559	-0.0279	-0.0074	0.0870	0.0370	0.0469	
$a_0^{f_0}$	0.5337	-0.2486	-0.0792	1	-0.7202	0.2599	0.4581	-0.2052	-0.0146	0.4734	-0.2798	-0.0031	0.3860	-0.2266	-0.0115	-0.2781	0.0048	
$a_1^{f_0}$	-0.2670	0.1617	0.0267	-0.7202	1	-0.6947	-0.2404	0.1415	0.0128	-0.2964	0.2603	-0.0377	-0.2410	0.1694	0.0090	0.2610	-0.0279	
$a_2^{f_0}$	-0.0922	0.0653	0.2795	0.2599	-0.6947	1	0.0190	-0.0056	0.0297	-0.0019	-0.0529	0.1086	-0.0081	-0.0097	0.0664	-0.0568	0.0874	
$a_0^{f_\perp}$	0.5121	-0.2526	-0.0035	0.4581	-0.2404	0.0190	1	-0.7672	0.1031	0.3418	-0.1831	-0.0539	0.4313	-0.2713	0.0163	-0.1994	-0.0127	
$a_1^{f_\perp}$	-0.2469	0.1671	-0.0120	-0.2052	0.1415	-0.0056	-0.7672	1	-0.5040	-0.1983	0.1259	0.0378	-0.2429	0.1907	-0.0274	0.1347	0.0083	
$a_2^{f_\perp}$	-0.0180	0.0056	0.0425	-0.0146	0.0128	0.0297	0.1031	-0.5040	1	-0.0271	0.0045	0.0524	-0.0286	0.0090	0.0530	0.0120	0.0187	
$a_0^{g_\perp, g^+}$	0.3774	-0.2177	-0.0562	0.4734	-0.2964	-0.0019	0.3418	-0.1983	-0.0271	1	-0.6751	0.2299	0.5903	-0.2849	-0.0084	-0.6325	0.1314	
$a_1^{g_\perp, g^+}$	-0.2148	0.1480	0.0382	-0.2798	0.2603	-0.0529	-0.1831	0.1259	0.0045	-0.6751	1	-0.6972	-0.2576	0.1666	-0.0268	0.6832	-0.1976	
$a_2^{g_\perp, g^+}$	-0.0472	0.0287	0.0559	-0.0031	-0.0377	0.1086	-0.0539	0.0378	0.0524	0.2299	-0.6972	1	-0.0760	0.0463	0.2693	-0.3207	0.2419	
$a_0^{g_0}$	0.4420	-0.2496	-0.0279	0.3860	-0.2410	-0.0081	0.4313	-0.2429	-0.0286	0.5903	-0.2576	-0.0760	1	-0.7868	0.3673	-0.2892	-0.0105	
$a_1^{g_0}$	-0.2680	0.1849	-0.0074	-0.2266	0.1694	-0.0097	-0.2713	0.1907	0.0090	-0.2849	0.1666	0.0463	-0.7868	1	-0.7393	0.1798	0.0107	
$a_2^{g_0}$	0.0018	-0.0169	0.0870	-0.0115	0.0090	0.0664	0.0163	-0.0274	0.0530	-0.0084	-0.0268	0.2693	0.3673	-0.7393	1	0.0302	0.0637	
$a_0^{g_\perp}$	-0.2284	0.1534	0.0370	-0.2781	0.2610	-0.0568	-0.1994	0.1347	0.0120	-0.6325	0.6832	-0.3207	-0.2892	0.1798	0.0302	1	-0.6223	
$a_1^{g_\perp}$	-0.0231	0.0147	0.0469	0.0048	-0.0279	0.0874	-0.0127	0.0083	0.0187	0.1314	-0.1976	0.2419	-0.0105	0.0107	0.0637	-0.6223	1	
$\Lambda_b \rightarrow \Lambda_c$	$a_0^{f^+}$	$a_1^{f^+}$	$a_2^{f^+}$	$a_0^{f_0}$	$a_1^{f_0}$	$a_2^{f_0}$	$a_0^{f_\perp}$	$a_1^{f_\perp}$	$a_2^{f_\perp}$	$a_0^{g_\perp, g^+}$	$a_1^{g_\perp, g^+}$	$a_2^{g_\perp, g^+}$	$a_0^{g_0}$	$a_1^{g_0}$	$a_2^{g_0}$	$a_0^{g_\perp}$	$a_1^{g_\perp}$	$a_2^{g_\perp}$
$a_0^{f^+}$	1	-0.5220	0.1623	0.7106	-0.2661	-0.0293	0.6259	-0.2683	0.0077	0.1992	-0.1307	-0.0277	0.2833	-0.1838	0.0436	-0.1611	0.0088	
$a_1^{f^+}$	-0.5220	1	-0.6595	-0.3199	0.4277	0.0649	-0.2548	0.2618	-0.0102	-0.1403	0.1878	0.0413	-0.1575	0.1932	-0.0364	0.1703	0.0030	
$a_2^{f^+}$	0.1623	-0.6595	1	-0.0350	0.1309	0.0939	0.0181	-0.0149	0.0300	-0.0111	0.0190	0.0007	0.0005	-0.0041	0.0186	0.0246	0.0088	
$a_0^{f_0}$	0.7106	-0.3199	-0.0350	1	-0.5132	0.1123	0.5190	-0.2037	-0.0014	0.2531	-0.2100	0.0128	0.2012	-0.1481	0.0096	-0.2057	-0.0079	
$a_1^{f_0}$	-0.2661	0.4277	0.1309	-0.5132	1	-0.5243	-0.1791	0.2285	0.0094	-0.1770	0.2589	0.0134	-0.1266	0.1854	-0.0086	0.2339	0.0127	
$a_2^{f_0}$	-0.0293	0.0649	0.0939	0.1123	-0.5243	1	-0.0222	0.0275	0.0138	0.0044	-0.0148	0.0300	-0.0074	0.0112	-0.0034	-0.0218	0.0075	
$a_0^{f_\perp}$	0.6259	-0.2548	0.0181	0.5190	-0.1791	-0.0222	1	-0.5829	0.1142	0.1754	-0.1255	-0.0168	0.2874	-0.1811	0.0416	-0.1320	-0.0086	
$a_1^{f_\perp}$	-0.2683	0.2618	-0.0149	-0.2037	0.2285	0.0275	-0.5829	1	-0.4656	-0.1154	0.1472	0.0360	-0.1487	0.1650	-0.0341	0.1319	0.0096	
$a_2^{f_\perp}$	0.0077	-0.0102	0.0300	-0.0014	0.0094	0.0138	0.1142	-0.4656	1	-0.0006	-0.0003	0.0057	0.0049	-0.0059	0.0087	-0.0006	0.0033	
$a_0^{g_\perp, g^+}$	0.1992	-0.1403	-0.0111	0.2531	-0.1770	0.0044	0.1754	-0.1154	-0.0006	1	-0.4436	0.0876	0.7054	-0.2594	0.0128	-0.4268	0.0479	
$a_1^{g_\perp, g^+}$	-0.1307	0.1878	0.0190	-0.2100	0.2589	-0.0148	-0.1255	0.1472	-0.0003	-0.4436	1	-0.5465	-0.2790	0.3438	0.0541	0.4776	-0.1381	
$a_2^{g_\perp, g^+}$	-0.0277	0.0413	0.0007	0.0128	0.0134	0.0300	-0.0168	0.0360	0.0057	0.0876	-0.5465	1	-0.0447	0.1194	0.0577	-0.1482	0.2692	
$a_0^{g_0}$	0.2833	-0.1575	0.0005	0.2012	-0.1266	-0.0074	0.2874	-0.1487	0.0049	0.7054	-0.2790	-0.0447	1	-0.5511	0.2196	-0.3015	0.0059	
$a_1^{g_0}$	-0.1838	0.1932	-0.0041	-0.1481	0.1854	0.0112	-0.1811	0.1650	-0.0059	-0.2594	0.3438	0.1194	-0.5511	1	-0.7687	0.2440	0.0190	
$a_2^{g_0}$	0.0436	-0.0364	0.0186	0.0096	-0.0086	-0.0034	0.0416	-0.0341	0.0087	0.0128	0.0541	0.0577	0.2196	-0.7687	1	0.0004	0.0405	
$a_0^{g_\perp}$	-0.1611	0.1703	0.0246	-0.2057	0.2339	-0.0218	-0.1320	0.1319	-0.0006	-0.4268	0.4776	-0.1482	-0.3015	0.2440	0.0004	1	-0.5028	
$a_1^{g_\perp}$	0.0088	0.0030	0.0088	-0.0079	0.0127	0.0075	-0.0086	0.0096	0.0033	0.0479	-0.1381	0.2692	0.0059	0.0190	0.0405	-0.5028	1	

TABLE XI. Correlation matrices of the higher-order form factor parameters for $\Lambda_b \rightarrow p$ (top) and $\Lambda_b \rightarrow \Lambda_c$ (bottom).

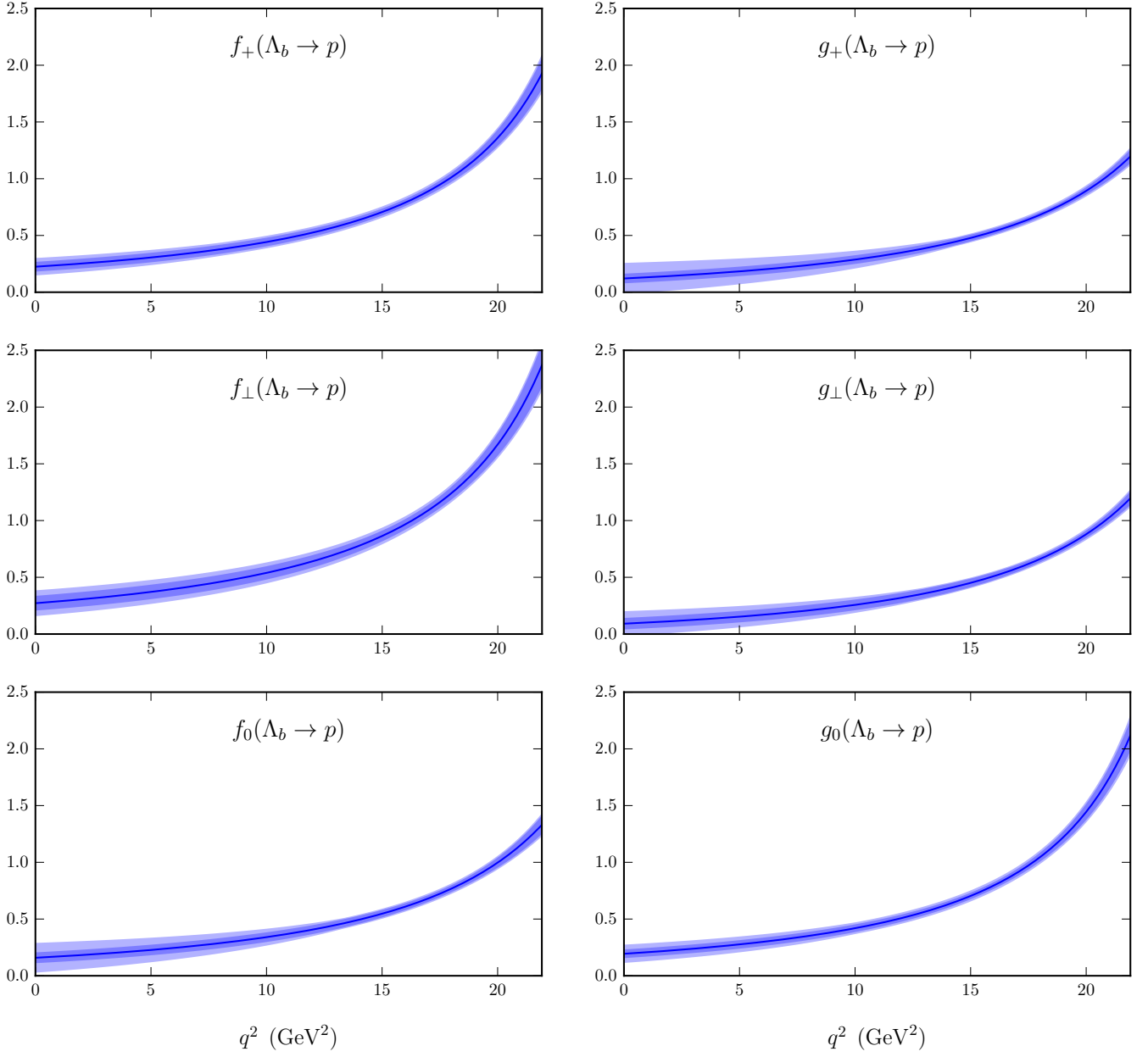


FIG. 10. Final results for the $\Lambda_b \rightarrow p$ form factors. The inner bands show the statistical uncertainty and the outer bands show the total uncertainty.

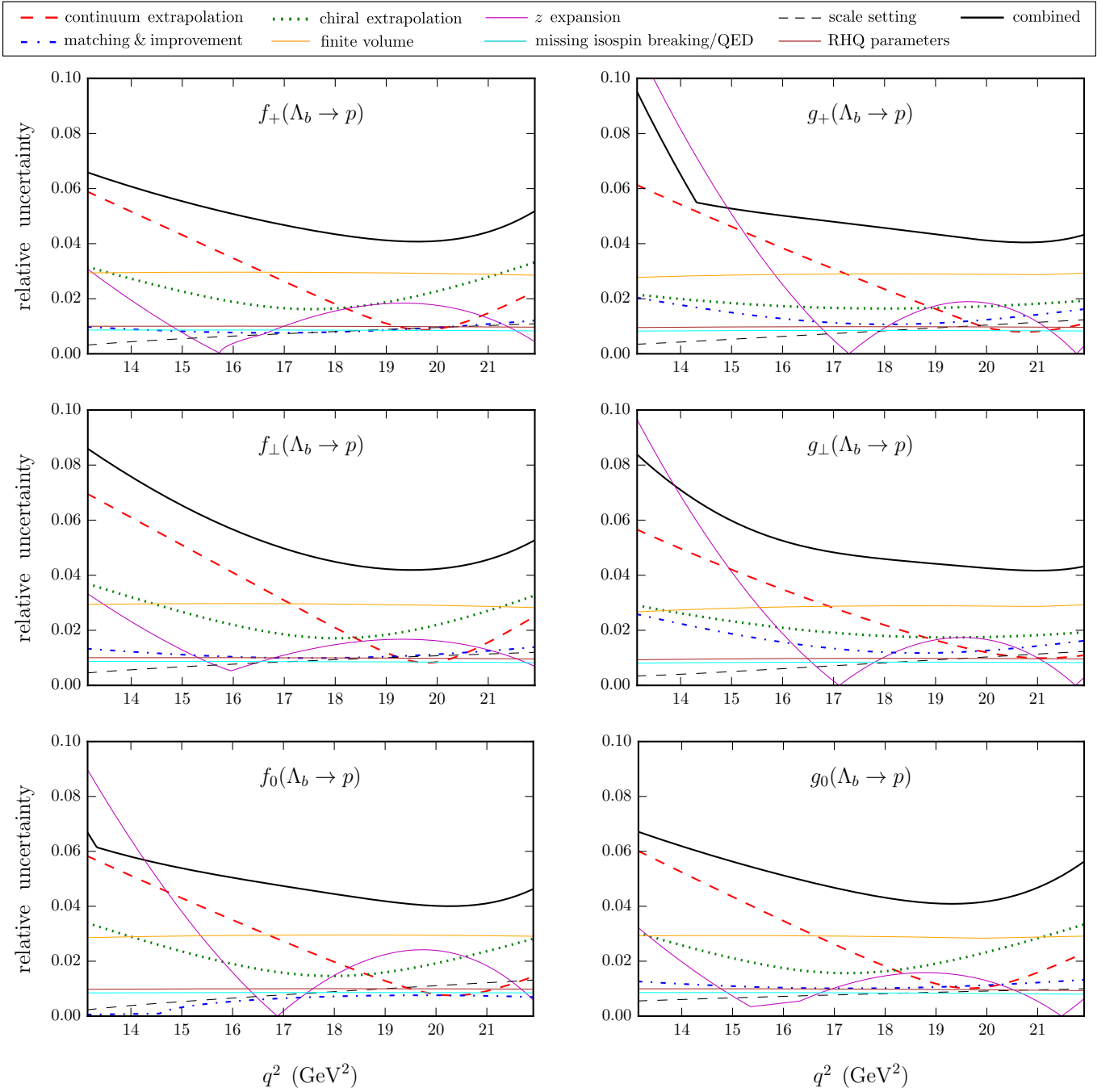


FIG. 11. Systematic uncertainties in the $\Lambda_b \rightarrow p$ form factors in the high- q^2 region. As explained in the main text, the combined uncertainty is not simply the quadratic sum of the individual uncertainties.

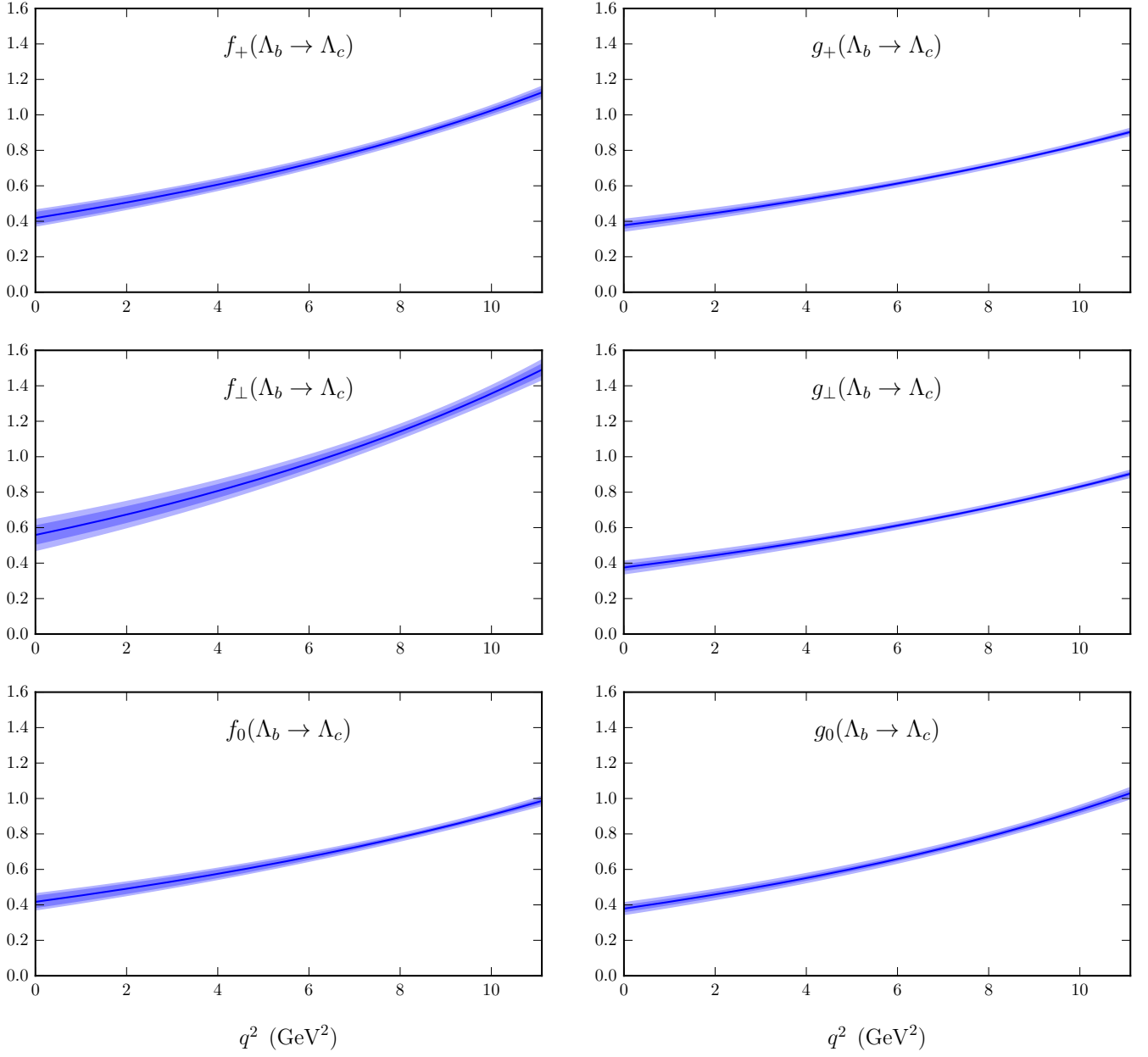


FIG. 12. Final results for the $\Lambda_b \rightarrow \Lambda_c$ form factors. The inner bands show the statistical uncertainty and the outer bands show the total uncertainty.

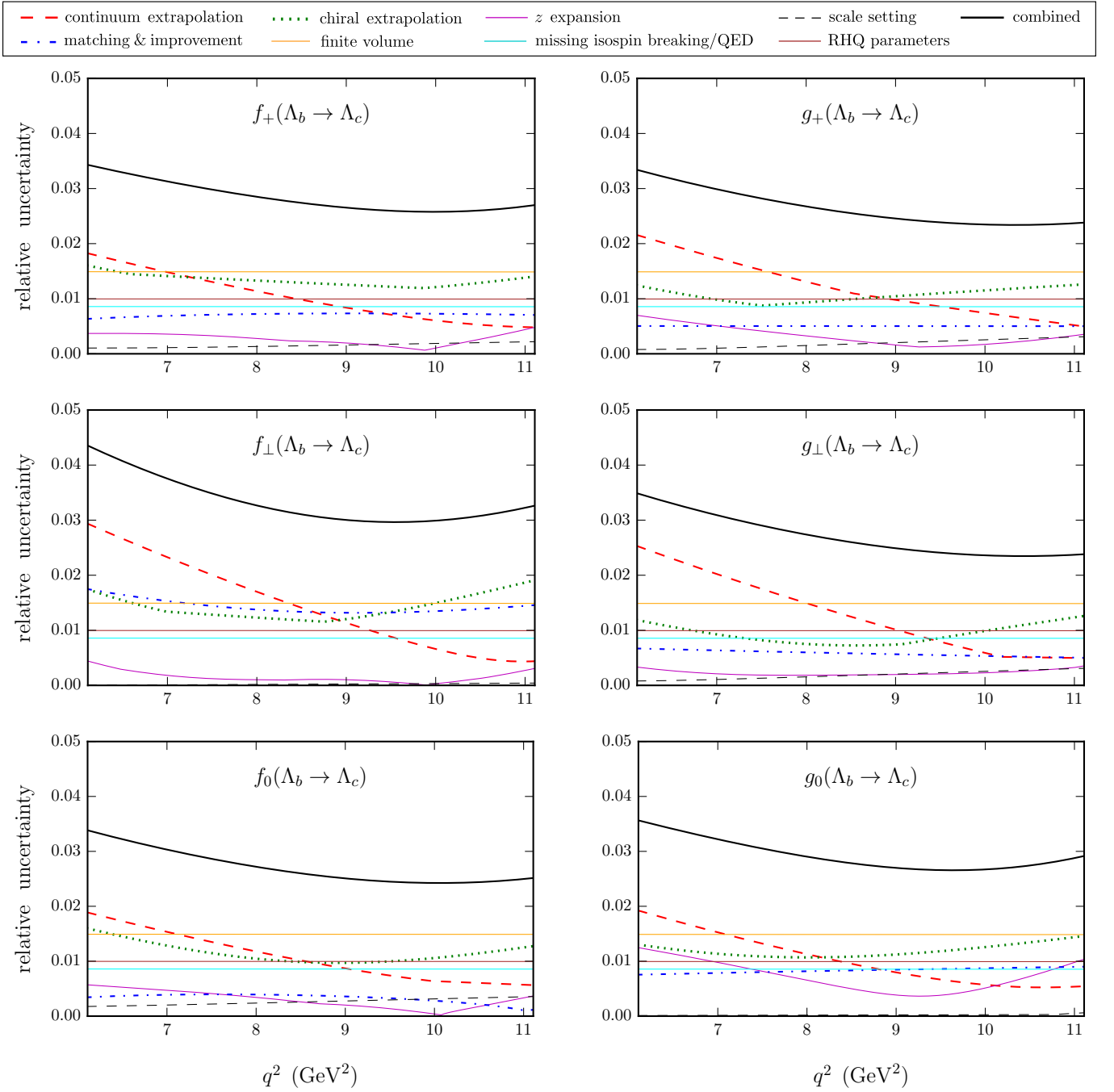


FIG. 13. Systematic uncertainties in the $\Lambda_b \rightarrow \Lambda_c$ form factors in the high- q^2 region. As explained in the main text, the combined uncertainty is not simply the quadratic sum of the individual uncertainties.

VI. PREDICTIONS FOR THE $\Lambda_b \rightarrow p \ell^- \bar{\nu}_\ell$ AND $\Lambda_b \rightarrow \Lambda_c \ell^- \bar{\nu}_\ell$ DECAY RATES

In this section, we present predictions for the $\Lambda_b \rightarrow p \ell^- \bar{\nu}_\ell$ and $\Lambda_b \rightarrow \Lambda_c \ell^- \bar{\nu}_\ell$ differential and integrated decay rates using our form factor results. Including possible right-handed currents with real-valued ϵ_q^R , the effective Hamiltonian in Eq. (2) leads to the following expression for the differential decay rate in terms of the helicity form factors,

$$\begin{aligned} \frac{d\Gamma}{dq^2} &= \frac{G_F^2 |V_{qb}^L|^2 \sqrt{s_+ s_-}}{768 \pi^3 m_{\Lambda_b}^3} \left(1 - \frac{m_\ell^2}{q^2}\right)^2 \\ &\times \left\{ 4(m_\ell^2 + 2q^2) \left(s_+ [(1 - \epsilon_q^R) g_\perp]^2 + s_- [(1 + \epsilon_q^R) f_\perp]^2 \right) \right. \\ &\quad + 2 \frac{m_\ell^2 + 2q^2}{q^2} \left(s_+ [(m_{\Lambda_b} - m_X)(1 - \epsilon_q^R) g_+]^2 + s_- [(m_{\Lambda_b} + m_X)(1 + \epsilon_q^R) f_+]^2 \right) \\ &\quad \left. + \frac{6m_\ell^2}{q^2} \left(s_+ [(m_{\Lambda_b} - m_X)(1 + \epsilon_q^R) f_0]^2 + s_- [(m_{\Lambda_b} + m_X)(1 - \epsilon_q^R) g_0]^2 \right) \right\}, \end{aligned} \quad (85)$$

where, as before, $X = p, \Lambda_c$ denotes the final-state baryon, and

$$s_\pm = (m_{\Lambda_b} \pm m_X)^2 - q^2. \quad (86)$$

Expressions for the individual helicity amplitudes and the angular distributions can be found in Refs. [27, 28, 70]. By combining experimental data with our form factor results, novel constraints in the (V_{qb}^L, ϵ_q^R) plane can be obtained.

In the following, we consider the Standard Model with $V_{qb}^L = V_{qb}$ and $\epsilon_q^R = 0$. Our predictions of the $\Lambda_b \rightarrow p \ell^- \bar{\nu}_\ell$ and $\Lambda_b \rightarrow \Lambda_c \ell^- \bar{\nu}_\ell$ differential decay rates for $\ell = e, \mu, \tau$ are shown in Figs. 14 and 15. The central values, statistical uncertainties, and systematic uncertainties have been calculated using Eq. (84); all baryon and lepton masses were taken from Ref. [1]. Our results are most precise in the high- q^2 region, where the form factor shapes are most tightly constrained by the lattice QCD data. We obtain the following partially integrated decay rates

$$\zeta_{p\mu\bar{\nu}}(15 \text{ GeV}^2) \equiv \frac{1}{|V_{ub}|^2} \int_{15 \text{ GeV}^2}^{q_{\text{max}}^2} \frac{d\Gamma(\Lambda_b \rightarrow p \mu^- \bar{\nu}_\mu)}{dq^2} dq^2 = (12.31 \pm 0.76 \pm 0.77) \text{ ps}^{-1}, \quad (87)$$

$$\zeta_{\Lambda_c\mu\bar{\nu}}(7 \text{ GeV}^2) \equiv \frac{1}{|V_{cb}|^2} \int_{7 \text{ GeV}^2}^{q_{\text{max}}^2} \frac{d\Gamma(\Lambda_b \rightarrow \Lambda_c \mu^- \bar{\nu}_\mu)}{dq^2} dq^2 = (8.37 \pm 0.16 \pm 0.34) \text{ ps}^{-1}, \quad (88)$$

and their ratio

$$\frac{\zeta_{p\mu\bar{\nu}}(15 \text{ GeV}^2)}{\zeta_{\Lambda_c\mu\bar{\nu}}(7 \text{ GeV}^2)} = 1.471 \pm 0.095 \pm 0.109, \quad (89)$$

where the first uncertainty is statistical and the second uncertainty is systematic. Together with experimental data, Eqs. (87), (88), and (89) will allow determinations of $|V_{ub}|$, $|V_{cb}|$, and $|V_{ub}/V_{cb}|$ with theory uncertainties of 4.4%, 2.2%, and 4.9%, respectively. A breakdown of the uncertainties into the individual sources, obtained by applying Eq. (84) to the various additional form factor fits discussed at the end of Sec. V, is given in Table XII.

The predicted total decay rates for all possible lepton flavors are

$$\Gamma(\Lambda_b \rightarrow p e^- \bar{\nu}_e) / |V_{ub}|^2 = (25.7 \pm 2.6 \pm 4.6) \text{ ps}^{-1} \quad (90)$$

$$\Gamma(\Lambda_b \rightarrow p \mu^- \bar{\nu}_\mu) / |V_{ub}|^2 = (25.7 \pm 2.6 \pm 4.6) \text{ ps}^{-1}, \quad (91)$$

$$\Gamma(\Lambda_b \rightarrow p \tau^- \bar{\nu}_\tau) / |V_{ub}|^2 = (17.7 \pm 1.3 \pm 1.6) \text{ ps}^{-1}, \quad (92)$$

$$\Gamma(\Lambda_b \rightarrow \Lambda_c e^- \bar{\nu}_e) / |V_{cb}|^2 = (21.5 \pm 0.8 \pm 1.1) \text{ ps}^{-1}, \quad (93)$$

$$\Gamma(\Lambda_b \rightarrow \Lambda_c \mu^- \bar{\nu}_\mu) / |V_{cb}|^2 = (21.5 \pm 0.8 \pm 1.1) \text{ ps}^{-1}, \quad (94)$$

$$\Gamma(\Lambda_b \rightarrow \Lambda_c \tau^- \bar{\nu}_\tau) / |V_{cb}|^2 = (7.15 \pm 0.15 \pm 0.27) \text{ ps}^{-1}. \quad (95)$$

Motivated by the $\mathcal{R}(D^{(*)})$ puzzle [14], we also provide predictions for the following ratios:

$$\frac{\Gamma(\Lambda_b \rightarrow \Lambda_c \tau^- \bar{\nu}_\tau)}{\Gamma(\Lambda_b \rightarrow \Lambda_c e^- \bar{\nu}_e)} = 0.3318 \pm 0.0074 \pm 0.0070, \quad (96)$$

$$\frac{\Gamma(\Lambda_b \rightarrow \Lambda_c \tau^- \bar{\nu}_\tau)}{\Gamma(\Lambda_b \rightarrow \Lambda_c \mu^- \bar{\nu}_\mu)} = 0.3328 \pm 0.0074 \pm 0.0070. \quad (97)$$

QED corrections to the decay rates, which may be relevant at this level of precision, have been neglected here.

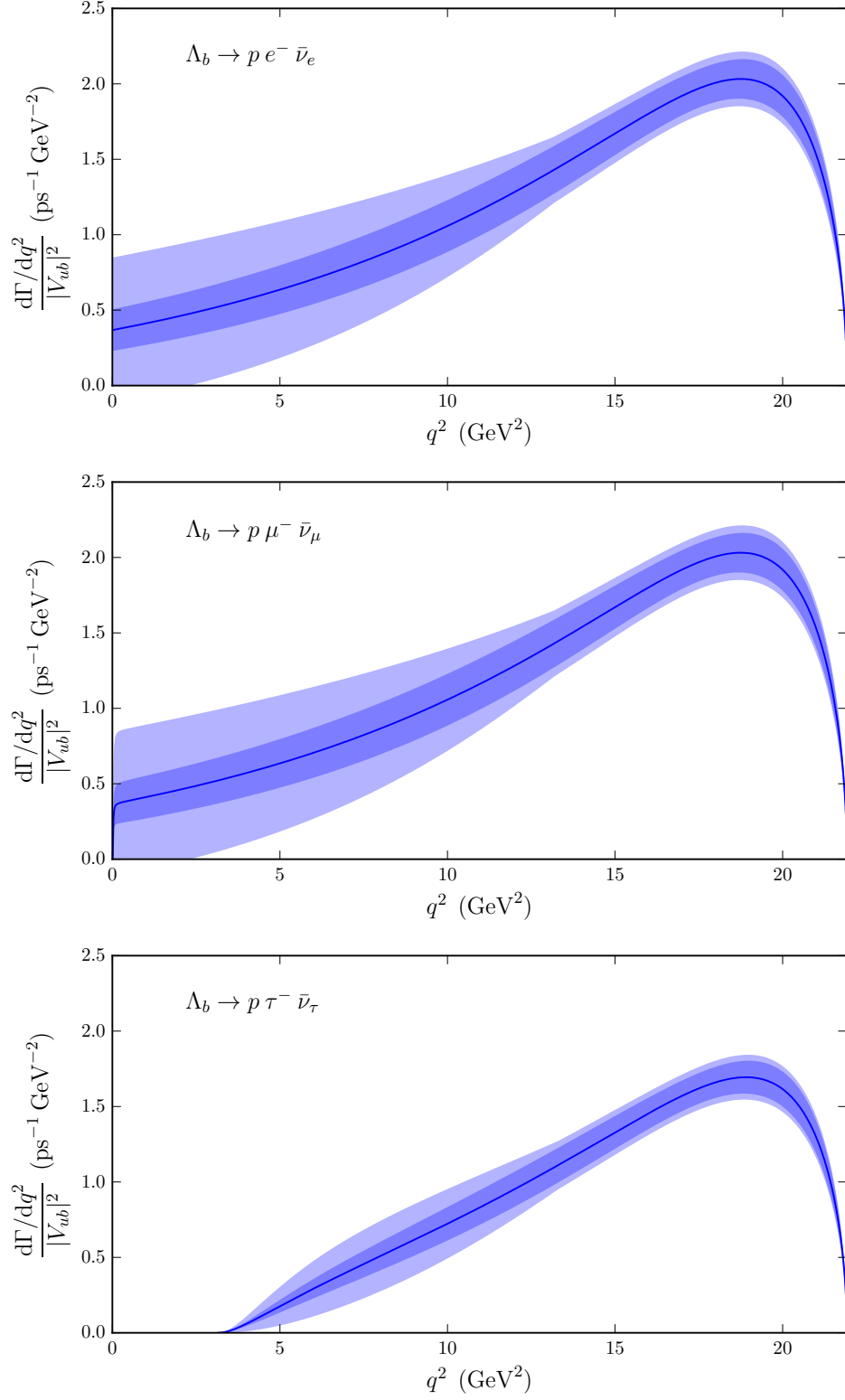


FIG. 14. Predictions for the $\Lambda_b \rightarrow p \ell^- \bar{\nu}_\ell$ differential decay rates for $\ell = e, \mu, \tau$ in the Standard Model. The inner bands show the statistical uncertainty and the outer bands show the total uncertainty, calculated using Eq. (84).

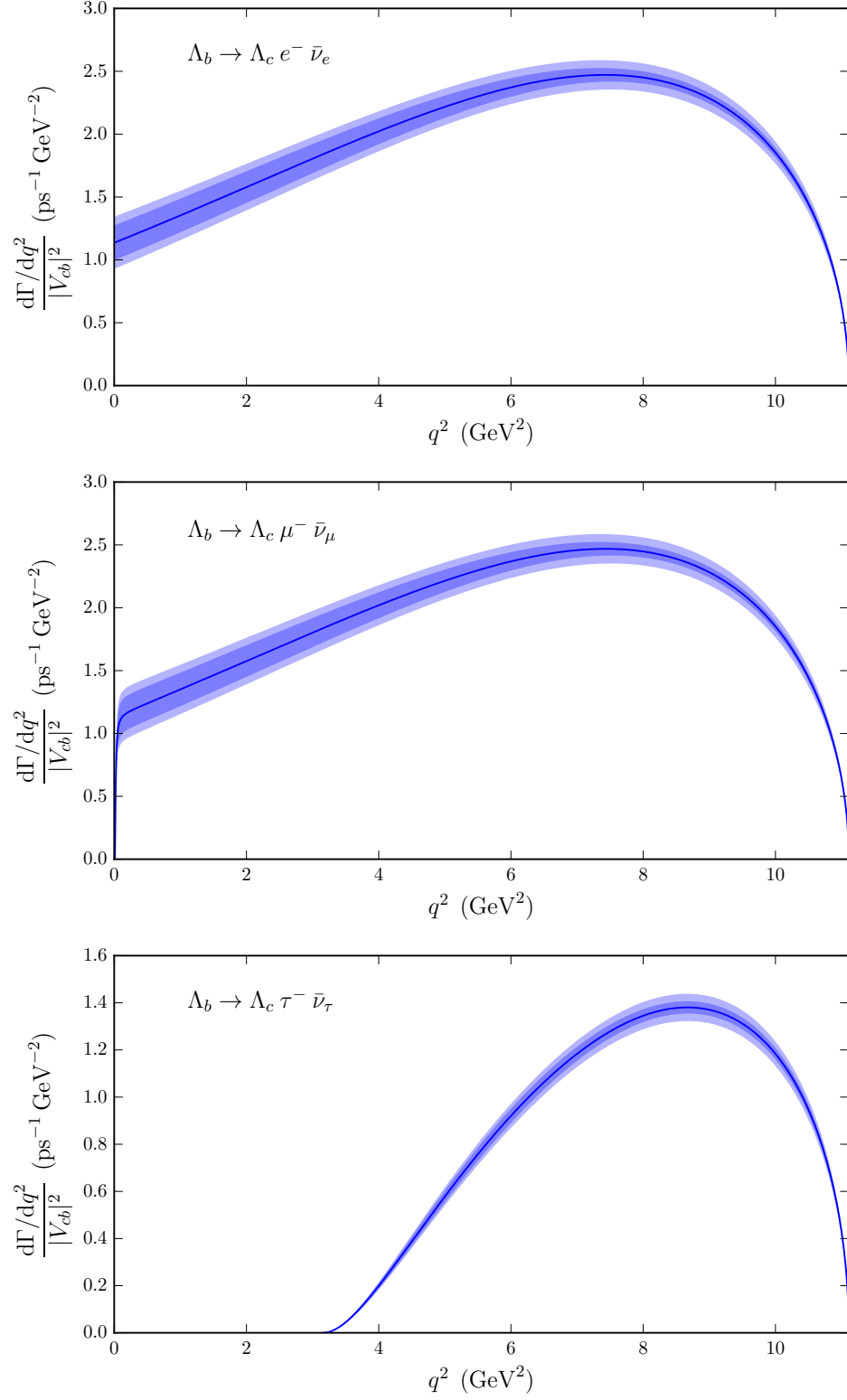


FIG. 15. Predictions for the $\Lambda_b \rightarrow \Lambda_c \ell^- \bar{\nu}_\ell$ differential decay rates for $\ell = e, \mu, \tau$ in the Standard Model. The inner bands show the statistical uncertainty and the outer bands show the total uncertainty, calculated using Eq. (84).

	$\zeta_{p\mu\bar{\nu}}(15 \text{ GeV}^2)$	$\zeta_{\Lambda_c\mu\bar{\nu}}(7 \text{ GeV}^2)$	$\frac{\zeta_{p\mu\bar{\nu}}(15 \text{ GeV}^2)}{\zeta_{\Lambda_c\mu\bar{\nu}}(7 \text{ GeV}^2)}$
Statistics	6.2	1.9	6.5
Finite volume	5.0	2.5	4.9
Continuum extrapolation	3.0	1.4	2.8
Chiral extrapolation	2.6	1.8	2.6
RHQ parameters	1.4	1.7	2.3
Matching & improvement	1.7	0.9	2.1
Missing isospin breaking/QED	1.2	1.4	2.0
Scale setting	1.7	0.3	1.8
z expansion	1.2	0.2	1.3
Total	8.8	4.5	9.8

TABLE XII. Approximate breakdown of relative uncertainties (in %) in the partially integrated $\Lambda_b \rightarrow p\mu^-\bar{\nu}_\mu$ and $\Lambda_b \rightarrow \Lambda_c\mu^-\bar{\nu}_\mu$ decay rates and their ratio, defined in Eqs. (87), (88), and (89). As explained in the main text, the combined uncertainty is not simply the quadratic sum of the individual uncertainties.

VII. SUMMARY

We have presented a high-precision lattice QCD calculation of the complete set of relativistic form factors describing the $\Lambda_b \rightarrow p$ and $\Lambda_b \rightarrow \Lambda_c$ matrix elements of the vector and axial vector $b \rightarrow u$ and $b \rightarrow c$ currents. The form factors and their uncertainties in the physical limit are shown in Figs. 10 and 12. Any observable depending on the form factors can be calculated using Eq. (84), which is based on two different sets of form factor parameters. The “nominal” form factors are used to calculate the central value and statistical uncertainty of the observable, and are given by the functions (79) with parameters and correlation matrices from Tables VIII and IX, together with the pole masses from Table VII. The “higher order” form factors are additionally needed to calculate the systematic uncertainty of the observable, and are given by Eq. (81) with the parameters from Tables X and XI. The higher-order fit was performed in such a way that the systematic uncertainty obtained from Eq. (84) includes the continuum extrapolation uncertainty, the chiral extrapolation uncertainty, the kinematic (q^2) extrapolation uncertainty, the perturbative matching/improvement uncertainty, the uncertainty due to the finite lattice volume, and the uncertainty from the missing isospin breaking effects. The individual contributions to the systematic uncertainties in the form factors are shown in Figs. 11 and 13.

Our predictions of the $\Lambda_b \rightarrow p\ell^-\bar{\nu}_\ell$ and $\Lambda_b \rightarrow \Lambda_c\ell^-\bar{\nu}_\ell$ differential decay rates using the new form factors are presented in Sec. VI. The results (87), (88), and (89) for the $\Lambda_b \rightarrow p\mu^-\bar{\nu}_\mu$ and $\Lambda_b \rightarrow \Lambda_c\mu^-\bar{\nu}_\mu$ differential decay rates in the high- q^2 region can be combined with forthcoming experimental data to determine $|V_{ub}|$, $|V_{cb}|$, and $|V_{ub}/V_{cb}|$ with theory uncertainties of 4.4%, 2.2%, and 4.9%, respectively. These uncertainties are competitive with the total uncertainties in the 2014 PDG values based on exclusive B meson decays [see Eq. (1)]. Compared to Ref. [29], we have reduced the uncertainty in the $\Lambda_b \rightarrow p\ell^-\bar{\nu}_\ell$ decay rate at high q^2 by a factor of 3. This reduction in uncertainty mainly resulted from the elimination of the static approximation for the b quark. Combined with experimental data, our form factor results will also provide novel constraints on right-handed couplings beyond the Standard Model [7–10]. The constraints from the baryonic decays nicely complement existing constraints from mesonic decays due to the unique dependence of the baryonic decays on ϵ_R . Using our $\Lambda_b \rightarrow \Lambda_c$ form factors, very precise predictions can also be made for the decay $\Lambda_b \rightarrow \Lambda_c\tau^-\bar{\nu}_\tau$, which may provide new insights into the $\mathcal{R}(D^{(*)})$ puzzle [28, 70].

ACKNOWLEDGMENTS

We thank William Sutcliffe, Ulrik Egede, and Patrick Owen for numerous discussions about the analysis of the decays $\Lambda_b \rightarrow p\mu\bar{\nu}_\mu$ and $\Lambda_b \rightarrow \Lambda_c\mu\bar{\nu}_\mu$ using LHCb data, and Gil Paz for comments regarding the z expansion. We are grateful to the RBC and UKQCD collaborations for making their gauge field configurations available. The lattice calculations were carried out using the Chroma software [71] on high-performance computing resources provided by XSEDE (supported by National Science Foundation Grant Number OCI-1053575) and NERSC (supported by U.S. Department of Energy Grant Number DE-AC02-05CH11231). SM is supported by the RHIC Physics Fellow Program of the RIKEN BNL Research Center. WD is supported by the U.S. Department of Energy Early Career Research Award DE-SC0010495 and the Solomon Buchsbaum Fund at MIT. CL is supported by the U.S. Department of Energy contract DE-AC02-98CH10886(BNL).

NOTE ADDED

After the completion of this work, a measurement of the ratio of partially integrated $\Lambda_b \rightarrow p\mu^-\bar{\nu}_\mu$ and $\Lambda_b \rightarrow \Lambda_c\mu^-\bar{\nu}_\mu$ decay rates was published by the LHCb Collaboration, with the result [72]

$$\frac{\int_{15 \text{ GeV}^2}^{q_{\text{max}}^2} \frac{d\Gamma(\Lambda_b \rightarrow p\mu^-\bar{\nu}_\mu)}{dq^2} dq^2}{\int_7 \text{ GeV}^2}^{q_{\text{max}}^2} \frac{d\Gamma(\Lambda_b \rightarrow \Lambda_c\mu^-\bar{\nu}_\mu)}{dq^2} dq^2 = (1.00 \pm 0.04 \pm 0.08) \times 10^{-2}, \quad (98)$$

where the first uncertainty is statistical and the second uncertainty is systematic. Combined with our lattice QCD result in Eq. (89), this gives [72]

$$\frac{|V_{ub}|}{|V_{cb}|} = 0.083 \pm 0.004(\text{expt}) \pm 0.004(\text{lattice}), \quad (99)$$

and, taking the value of $|V_{cb}|$ extracted from exclusive B decays [72],

$$|V_{ub}| = (3.27 \pm 0.15(\text{expt}) \pm 0.16(\text{lattice}) \pm 0.06(|V_{cb}|)) \times 10^{-3}. \quad (100)$$

Appendix A: Tables of lattice form factor data

$f(\Lambda_b \rightarrow p)$	$ \mathbf{p}' ^2/(2\pi/L)^2$	C14	C24	C54	F23	F43	F63
f_+	1	1.436(60)	1.417(52)	1.429(54)	1.422(60)	1.419(51)	1.436(41)
	2	1.209(66)	1.202(59)	1.213(55)	1.210(83)	1.218(57)	1.236(44)
	3	1.037(73)	1.037(52)	1.050(50)	1.032(56)	1.051(36)	1.083(34)
	4	0.912(64)	0.925(27)	0.938(27)	0.968(31)	0.964(22)	0.969(19)
	5	0.809(34)	0.823(26)	0.836(26)	0.856(30)	0.857(22)	0.875(19)
	6	0.740(34)	0.754(26)	0.768(26)	0.780(29)	0.788(22)	0.810(19)
	8	0.614(35)	0.651(27)	0.664(27)	0.682(29)	0.690(21)	0.710(19)
	9	0.590(36)	0.608(28)	0.623(27)	0.655(29)	0.649(22)	0.672(19)
	f_\perp	1	1.767(88)	1.762(64)	1.802(66)	1.780(81)	1.771(73)
2		1.526(85)	1.523(68)	1.558(64)	1.547(97)	1.554(71)	1.582(50)
3		1.32(11)	1.325(85)	1.353(81)	1.31(11)	1.333(76)	1.390(57)
4		1.136(95)	1.156(61)	1.185(54)	1.201(57)	1.203(34)	1.224(46)
5		1.009(50)	1.024(39)	1.056(39)	1.068(45)	1.079(32)	1.112(29)
6		0.923(50)	0.941(39)	0.968(39)	0.964(44)	0.988(32)	1.029(29)
8		0.756(50)	0.805(40)	0.830(39)	0.839(45)	0.857(32)	0.893(30)
9		0.726(51)	0.754(41)	0.781(40)	0.808(46)	0.811(33)	0.849(31)
f_0		1	1.056(24)	1.011(26)	1.008(26)	1.051(29)	1.040(24)
	2	0.887(37)	0.878(34)	0.874(37)	0.889(43)	0.894(36)	0.891(36)
	3	0.775(39)	0.777(24)	0.777(24)	0.788(29)	0.796(24)	0.798(23)
	4	0.718(40)	0.727(25)	0.724(29)	0.757(49)	0.748(48)	0.746(20)
	5	0.654(24)	0.674(20)	0.672(20)	0.666(26)	0.669(21)	0.681(17)
	6	0.606(24)	0.631(20)	0.633(19)	0.626(25)	0.627(21)	0.645(17)
	8	0.516(26)	0.549(22)	0.555(20)	0.550(29)	0.555(24)	0.581(19)
	9	0.502(30)	0.529(28)	0.535(20)	0.530(29)	0.530(26)	0.559(21)
	g_+	1	0.952(17)	0.922(17)	0.920(14)	0.947(24)	0.939(23)
2		0.828(19)	0.815(17)	0.813(16)	0.823(27)	0.826(24)	0.821(21)
3		0.721(28)	0.721(19)	0.722(19)	0.721(33)	0.729(25)	0.735(22)
4		0.648(24)	0.664(16)	0.663(12)	0.665(27)	0.659(24)	0.663(21)
5		0.582(20)	0.606(15)	0.606(11)	0.598(27)	0.600(27)	0.607(23)
6		0.540(20)	0.567(15)	0.569(11)	0.559(30)	0.561(31)	0.576(26)
8		0.463(22)	0.497(16)	0.505(12)	0.494(38)	0.496(36)	0.517(30)
9		0.458(25)	0.481(24)	0.489(12)	0.487(30)	0.483(30)	0.507(25)
g_\perp		1	0.952(23)	0.920(20)	0.919(16)	0.947(30)	0.939(28)
	2	0.827(25)	0.812(20)	0.811(18)	0.818(32)	0.822(30)	0.817(26)
	3	0.719(32)	0.720(22)	0.720(22)	0.715(38)	0.723(31)	0.729(27)
	4	0.643(29)	0.659(20)	0.658(16)	0.657(33)	0.651(30)	0.655(26)
	5	0.578(26)	0.603(19)	0.602(14)	0.586(34)	0.589(33)	0.598(28)
	6	0.535(27)	0.566(20)	0.566(15)	0.546(38)	0.549(37)	0.566(32)
	8	0.456(36)	0.495(24)	0.503(17)	0.476(51)	0.480(48)	0.506(40)
	9	0.454(39)	0.482(36)	0.491(17)	0.473(45)	0.470(45)	0.499(36)
	g_0	1	1.475(60)	1.469(47)	1.477(41)	1.496(75)	1.469(57)
2		1.237(44)	1.229(39)	1.242(36)	1.274(50)	1.262(42)	1.275(26)
3		1.055(24)	1.048(21)	1.065(21)	1.082(28)	1.089(22)	1.113(17)
4		0.912(22)	0.924(20)	0.935(19)	0.982(25)	0.972(19)	0.972(15)
5		0.808(21)	0.818(18)	0.833(19)	0.872(22)	0.867(17)	0.881(14)
6		0.734(21)	0.746(18)	0.759(19)	0.782(21)	0.789(17)	0.811(14)
8		0.603(30)	0.631(18)	0.646(19)	0.668(20)	0.675(17)	0.695(14)
9		0.576(24)	0.592(20)	0.607(20)	0.640(23)	0.638(18)	0.660(16)

TABLE XIII. $\Lambda_b \rightarrow p$ helicity form factors.

$f(\Lambda_b \rightarrow p)$	$ \mathbf{p}' ^2/(2\pi/L)^2$	C14	C24	C54	F23	F43	F63
f_1^V	1	1.168(42)	1.144(46)	1.152(47)	1.123(48)	1.138(37)	1.164(31)
	2	0.974(55)	0.968(54)	0.977(51)	0.952(75)	0.973(49)	1.000(41)
	3	0.846(49)	0.844(31)	0.858(31)	0.838(24)	0.860(20)	0.889(21)
	4	0.771(44)	0.782(19)	0.792(19)	0.816(24)	0.814(25)	0.819(15)
	5	0.692(25)	0.707(20)	0.715(20)	0.728(26)	0.729(21)	0.745(15)
	6	0.641(25)	0.654(19)	0.666(20)	0.677(23)	0.681(20)	0.698(15)
	8	0.547(26)	0.579(20)	0.590(20)	0.606(23)	0.611(19)	0.629(15)
	9	0.530(27)	0.545(21)	0.557(20)	0.587(23)	0.578(20)	0.597(15)
	f_2^V	1	0.505(46)	0.520(29)	0.543(25)	0.556(45)	0.532(39)
2		0.465(32)	0.466(28)	0.485(25)	0.503(39)	0.489(30)	0.485(23)
3		0.397(53)	0.405(48)	0.413(43)	0.397(78)	0.397(58)	0.417(32)
4		0.307(44)	0.315(47)	0.328(46)	0.325(54)	0.327(40)	0.337(40)
5		0.267(24)	0.267(20)	0.285(18)	0.288(29)	0.295(25)	0.306(18)
6		0.238(24)	0.241(20)	0.251(18)	0.243(28)	0.258(24)	0.276(18)
8		0.176(24)	0.190(20)	0.200(18)	0.198(29)	0.207(25)	0.220(19)
9		0.165(25)	0.175(21)	0.187(19)	0.187(30)	0.196(26)	0.210(20)
f_3^V		1	-0.145(59)	-0.172(46)	-0.188(42)	-0.092(64)	-0.127(43)
	2	-0.118(38)	-0.123(41)	-0.141(33)	-0.085(59)	-0.106(33)	-0.149(24)
	3	-0.101(37)	-0.095(39)	-0.116(34)	-0.072(41)	-0.091(31)	-0.131(25)
	4	-0.079(39)	-0.081(43)	-0.102(41)	-0.088(61)	-0.099(40)	-0.111(27)
	5	-0.059(33)	-0.051(34)	-0.068(31)	-0.097(39)	-0.094(29)	-0.100(28)
	6	-0.056(34)	-0.037(34)	-0.055(29)	-0.083(40)	-0.087(30)	-0.087(23)
	8	-0.056(44)	-0.054(42)	-0.064(33)	-0.101(48)	-0.101(38)	-0.086(29)
	9	-0.053(58)	-0.031(44)	-0.043(34)	-0.107(50)	-0.092(46)	-0.072(35)
	f_1^A	1	0.959(18)	0.957(19)	0.950(17)	0.953(21)	0.947(17)
2		0.846(18)	0.837(20)	0.838(17)	0.868(24)	0.868(22)	0.865(20)
3		0.731(13)	0.726(12)	0.738(13)	0.762(18)	0.769(16)	0.773(16)
4		0.668(14)	0.685(15)	0.687(13)	0.701(15)	0.696(13)	0.701(11)
5		0.598(12)	0.614(12)	0.621(12)	0.642(14)	0.639(12)	0.643(11)
6		0.554(12)	0.568(11)	0.576(11)	0.597(14)	0.599(15)	0.606(12)
8		0.480(21)	0.500(11)	0.508(14)	0.532(16)	0.531(13)	0.543(12)
9		0.467(16)	0.477(13)	0.487(16)	0.512(15)	0.508(14)	0.522(12)
f_2^A		1	0.008(39)	0.046(33)	0.039(29)	0.007(41)	0.010(37)
	2	0.024(38)	0.030(33)	0.034(34)	0.061(45)	0.057(40)	0.059(41)
	3	0.015(39)	0.007(30)	0.023(33)	0.058(52)	0.057(42)	0.055(41)
	4	0.030(40)	0.032(34)	0.036(29)	0.053(42)	0.056(37)	0.057(37)
	5	0.024(38)	0.012(29)	0.023(27)	0.068(40)	0.061(37)	0.056(34)
	6	0.023(39)	0.003(30)	0.012(27)	0.062(42)	0.061(38)	0.050(35)
	8	0.030(64)	0.006(35)	0.007(31)	0.068(55)	0.064(52)	0.046(42)
	9	0.017(53)	-0.006(45)	-0.004(35)	0.048(57)	0.048(57)	0.028(42)
	f_3^A	1	-0.98(12)	-0.976(89)	-1.033(80)	-1.01(15)	-0.99(12)
2		-0.77(10)	-0.784(98)	-0.829(94)	-0.79(12)	-0.78(11)	-0.844(79)
3		-0.672(44)	-0.676(39)	-0.702(32)	-0.654(53)	-0.667(43)	-0.732(33)
4		-0.532(43)	-0.526(37)	-0.558(31)	-0.605(53)	-0.601(42)	-0.610(32)
5		-0.479(40)	-0.471(35)	-0.501(29)	-0.520(48)	-0.521(40)	-0.561(31)
6		-0.429(40)	-0.428(34)	-0.452(29)	-0.437(45)	-0.457(40)	-0.504(31)
8		-0.323(41)	-0.350(36)	-0.372(30)	-0.353(47)	-0.379(42)	-0.412(33)
9		-0.299(43)	-0.318(37)	-0.340(31)	-0.348(50)	-0.358(44)	-0.391(35)

TABLE XIV. $\Lambda_b \rightarrow p$ Weinberg form factors.

$f(\Lambda_b \rightarrow \Lambda_c)$	$ \mathbf{p}' ^2/(2\pi/L)^2$	C14	C24	C54	F23	F43	F63
f_+	1	1.0401(82)	1.0114(81)	1.0170(77)	1.068(15)	1.062(13)	1.047(10)
	2	0.9887(74)	0.9613(76)	0.9676(72)	1.016(14)	1.011(12)	0.998(10)
	3	0.9418(69)	0.9167(73)	0.9229(69)	0.968(13)	0.963(12)	0.9528(95)
	4	0.9018(92)	0.8826(77)	0.8852(71)	0.936(13)	0.927(12)	0.9133(88)
	5	0.864(12)	0.8515(73)	0.8528(67)	0.894(17)	0.887(17)	0.876(14)
	6	0.8327(67)	0.820(11)	0.8202(81)	0.859(15)	0.852(14)	0.8455(96)
	8	0.7692(81)	0.757(12)	0.758(10)	0.799(15)	0.791(14)	0.788(11)
	9	0.7406(98)	0.727(14)	0.728(12)	0.766(15)	0.758(14)	0.757(12)
	10	0.7098(89)	0.709(16)	0.708(15)	0.748(18)	0.737(16)	0.735(14)
	f_\perp	1	1.467(17)	1.431(13)	1.450(17)	1.464(23)	1.458(16)
2		1.400(13)	1.368(12)	1.386(13)	1.398(19)	1.394(14)	1.390(13)
3		1.339(12)	1.308(12)	1.326(13)	1.335(17)	1.333(13)	1.330(12)
4		1.268(17)	1.244(12)	1.257(15)	1.282(18)	1.276(17)	1.270(17)
5		1.219(20)	1.204(12)	1.215(12)	1.228(18)	1.224(21)	1.218(21)
6		1.180(12)	1.163(13)	1.172(12)	1.185(15)	1.181(14)	1.176(11)
8		1.094(14)	1.078(18)	1.086(15)	1.103(19)	1.099(17)	1.102(16)
9		1.056(14)	1.039(19)	1.047(16)	1.055(18)	1.054(16)	1.061(16)
10		0.997(14)	1.000(23)	1.004(21)	1.021(22)	1.015(20)	1.027(20)
f_0		1	0.9025(45)	0.8952(57)	0.8937(54)	0.945(13)	0.9392(98)
	2	0.8674(41)	0.8598(54)	0.8586(51)	0.906(12)	0.8996(88)	0.8846(57)
	3	0.8336(38)	0.8273(50)	0.8258(48)	0.867(11)	0.8619(81)	0.8508(51)
	4	0.8032(46)	0.7935(61)	0.7920(58)	0.842(13)	0.8337(86)	0.8231(75)
	5	0.7748(41)	0.7714(46)	0.7692(43)	0.805(12)	0.8012(99)	0.7939(68)
	6	0.7458(46)	0.7429(53)	0.7409(53)	0.772(10)	0.7691(88)	0.7669(76)
	8	0.6970(70)	0.6928(75)	0.6924(78)	0.729(17)	0.723(13)	0.723(11)
	9	0.6716(69)	0.6655(68)	0.6655(70)	0.696(14)	0.691(11)	0.693(10)
	10	0.6582(84)	0.659(12)	0.658(12)	0.694(22)	0.685(18)	0.685(16)
	g_+	1	0.8397(32)	0.8334(62)	0.8318(56)	0.8724(73)	0.8673(57)
2		0.8069(33)	0.8024(70)	0.7998(56)	0.8426(71)	0.8361(54)	0.8173(30)
3		0.7777(30)	0.7738(58)	0.7718(53)	0.8099(66)	0.8031(49)	0.7887(29)
4		0.7527(26)	0.7498(68)	0.7476(54)	0.7783(58)	0.7728(43)	0.7633(28)
5		0.7268(28)	0.7232(56)	0.7217(50)	0.7503(56)	0.7442(42)	0.7378(30)
6		0.7023(34)	0.6978(59)	0.6965(53)	0.7208(57)	0.7155(49)	0.7147(32)
8		0.6595(45)	0.6537(65)	0.6536(56)	0.6731(65)	0.6680(54)	0.6732(45)
9		0.6402(52)	0.6311(72)	0.6319(70)	0.650(11)	0.6452(91)	0.6547(62)
10		0.6240(71)	0.624(11)	0.625(11)	0.641(10)	0.6352(87)	0.642(11)
g_\perp		1	0.8389(35)	0.8332(50)	0.8315(48)	0.8720(72)	0.8663(57)
	2	0.8054(37)	0.8016(67)	0.7989(52)	0.8415(72)	0.8347(57)	0.8167(34)
	3	0.7756(35)	0.7729(51)	0.7708(44)	0.8081(68)	0.8017(50)	0.7878(33)
	4	0.7511(32)	0.7500(64)	0.7472(55)	0.7775(56)	0.7714(42)	0.7634(32)
	5	0.7244(34)	0.7226(47)	0.7206(48)	0.7482(54)	0.7426(41)	0.7373(33)
	6	0.6983(41)	0.6958(50)	0.6944(45)	0.7159(56)	0.7116(47)	0.7120(33)
	8	0.6540(57)	0.6511(57)	0.6510(49)	0.6664(56)	0.6626(48)	0.6691(41)
	9	0.6335(58)	0.6275(67)	0.6284(56)	0.6408(94)	0.6374(81)	0.6495(52)
	10	0.6206(90)	0.6230(91)	0.6233(95)	0.637(11)	0.6325(88)	0.641(12)
	g_0	1	0.9771(97)	0.959(12)	0.9608(99)	1.007(15)	0.998(13)
2		0.9296(66)	0.913(11)	0.9151(88)	0.958(13)	0.951(11)	0.9292(75)
3		0.8866(63)	0.873(11)	0.8740(86)	0.916(12)	0.908(10)	0.8891(67)
4		0.8478(61)	0.838(11)	0.8383(86)	0.873(13)	0.866(13)	0.853(11)
5		0.8141(62)	0.804(11)	0.8044(86)	0.838(12)	0.831(10)	0.8197(88)
6		0.7854(66)	0.774(12)	0.7737(95)	0.807(12)	0.800(11)	0.7950(76)
8		0.7281(86)	0.716(14)	0.717(11)	0.745(15)	0.738(13)	0.7409(95)
9		0.704(11)	0.688(16)	0.690(14)	0.718(19)	0.712(16)	0.717(12)
10		0.6732(91)	0.676(18)	0.675(16)	0.698(18)	0.691(15)	0.695(13)

TABLE XV. $\Lambda_b \rightarrow \Lambda_c$ helicity form factors.

$f(\Lambda_b \rightarrow \Lambda_c)$	$ \mathbf{p}' ^2/(2\pi/L)^2$	C14	C24	C54	F23	F43	F63
f_1^V	1	0.9534(80)	0.9273(80)	0.9316(71)	0.988(15)	0.981(14)	0.965(11)
	2	0.9096(72)	0.8842(74)	0.8894(66)	0.943(14)	0.937(13)	0.923(11)
	3	0.8697(66)	0.8465(71)	0.8517(63)	0.902(13)	0.896(12)	0.8852(95)
	4	0.8390(82)	0.8214(75)	0.8230(65)	0.877(14)	0.867(12)	0.8527(88)
	5	0.807(11)	0.7950(70)	0.7957(60)	0.840(18)	0.832(16)	0.821(13)
	6	0.7798(63)	0.768(11)	0.7679(80)	0.810(16)	0.802(14)	0.7954(98)
	8	0.7255(78)	0.714(12)	0.7154(98)	0.758(15)	0.749(15)	0.746(11)
	9	0.7009(96)	0.688(13)	0.689(11)	0.730(15)	0.721(14)	0.719(12)
	10	0.6761(87)	0.676(15)	0.674(14)	0.716(19)	0.704(16)	0.700(14)
	f_2^V	1	0.365(11)	0.3569(91)	0.367(11)	0.338(18)	0.338(13)
2		0.3481(80)	0.3427(62)	0.3516(72)	0.323(13)	0.3241(87)	0.3308(73)
3		0.3330(67)	0.3273(56)	0.3354(60)	0.308(11)	0.3107(83)	0.3149(71)
4		0.3045(82)	0.2997(70)	0.3072(83)	0.287(11)	0.2903(86)	0.296(11)
5		0.2927(78)	0.2903(52)	0.2968(56)	0.2756(10)	0.2784(76)	0.2813(75)
6		0.2839(60)	0.2802(51)	0.2861(55)	0.2665(98)	0.2690(74)	0.2700(63)
8		0.2618(76)	0.2578(66)	0.2624(65)	0.244(11)	0.248(11)	0.2523(94)
9		0.2524(77)	0.2489(66)	0.2531(66)	0.231(11)	0.2363(10)	0.2422(90)
10		0.2279(75)	0.2300(88)	0.2330(78)	0.216(13)	0.221(11)	0.231(12)
f_3^V		1	-0.090(15)	-0.057(13)	-0.068(11)	-0.075(32)	-0.074(29)
	2	-0.078(14)	-0.045(12)	-0.057(10)	-0.070(31)	-0.070(28)	-0.072(20)
	3	-0.070(13)	-0.037(12)	-0.051(10)	-0.067(31)	-0.065(29)	-0.067(20)
	4	-0.073(14)	-0.057(13)	-0.064(11)	-0.072(31)	-0.067(28)	-0.060(19)
	5	-0.068(22)	-0.051(12)	-0.0572(97)	-0.074(41)	-0.065(40)	-0.058(31)
	6	-0.076(14)	-0.057(17)	-0.061(11)	-0.084(31)	-0.073(28)	-0.064(21)
	8	-0.072(17)	-0.054(21)	-0.058(14)	-0.075(50)	-0.066(44)	-0.057(28)
	9	-0.078(25)	-0.060(28)	-0.063(21)	-0.091(44)	-0.080(38)	-0.067(27)
	10	-0.051(17)	-0.049(20)	-0.048(15)	-0.063(54)	-0.053(46)	-0.042(29)
	f_1^A	1	0.8581(72)	0.838(12)	0.8386(87)	0.881(12)	0.890(10)
2		0.8235(57)	0.810(12)	0.8089(85)	0.853(10)	0.8514(86)	0.8242(58)
3		0.7918(53)	0.780(11)	0.7791(84)	0.822(10)	0.8126(84)	0.7948(58)
4		0.7608(51)	0.749(11)	0.7498(83)	0.7824(94)	0.7795(83)	0.7627(69)
5		0.7357(55)	0.726(11)	0.7255(84)	0.7579(96)	0.7502(81)	0.7397(67)
6		0.7144(56)	0.704(12)	0.7030(96)	0.7355(95)	0.7271(82)	0.7232(68)
8		0.6709(71)	0.659(13)	0.659(10)	0.687(12)	0.6791(98)	0.6818(88)
9		0.6519(90)	0.637(15)	0.638(14)	0.666(17)	0.659(14)	0.664(11)
10		0.6289(80)	0.626(16)	0.627(14)	0.647(14)	0.639(11)	0.643(12)
f_2^A		1	0.032(12)	0.008(15)	0.012(10)	0.016(18)	0.040(15)
	2	0.031(11)	0.014(15)	0.017(10)	0.020(15)	0.028(13)	0.013(12)
	3	0.027(11)	0.013(15)	0.014(10)	0.024(15)	0.018(12)	0.012(11)
	4	0.016(10)	-0.002(14)	0.0045(98)	0.008(16)	0.014(14)	-0.001(15)
	5	0.019(11)	0.005(15)	0.008(10)	0.016(15)	0.013(13)	0.004(14)
	6	0.027(12)	0.014(18)	0.015(13)	0.033(15)	0.026(13)	0.019(13)
	8	0.029(15)	0.013(24)	0.014(17)	0.034(18)	0.028(16)	0.022(15)
	9	0.031(17)	0.017(27)	0.016(21)	0.043(22)	0.037(20)	0.025(18)
	10	0.014(16)	0.006(20)	0.005(13)	0.016(20)	0.011(17)	0.003(15)
	f_3^A	1	-0.501(24)	-0.513(46)	-0.525(43)	-0.530(42)	-0.457(34)
2		-0.467(16)	-0.459(14)	-0.478(14)	-0.462(29)	-0.438(24)	-0.467(16)
3		-0.438(15)	-0.431(13)	-0.447(12)	-0.433(27)	-0.439(23)	-0.439(15)
4		-0.422(17)	-0.437(17)	-0.438(15)	-0.439(37)	-0.421(32)	-0.440(26)
5		-0.399(16)	-0.402(14)	-0.410(13)	-0.408(28)	-0.411(25)	-0.410(18)
6		-0.381(16)	-0.378(14)	-0.387(13)	-0.384(27)	-0.388(24)	-0.387(16)
8		-0.343(26)	-0.342(15)	-0.352(14)	-0.348(33)	-0.348(30)	-0.354(17)
9		-0.330(31)	-0.329(17)	-0.337(16)	-0.331(29)	-0.331(26)	-0.339(19)
10		-0.299(31)	-0.339(35)	-0.332(31)	-0.348(59)	-0.345(52)	-0.355(43)

TABLE XVI. $\Lambda_b \rightarrow \Lambda_c$ Weinberg form factors.

-
- [1] **Particle Data Group** Collaboration, K. Olive *et al.*, “Review of Particle Physics,” *Chin.Phys.* **C38** (2014) 090001.
- [2] J. A. Bailey, C. Bernard, C. E. DeTar, M. Di Pierro, A. El-Khadra, *et al.*, “The $B \rightarrow \pi \ell \nu$ semileptonic form factor from three-flavor lattice QCD: A Model-independent determination of $|V_{ub}|$,” *Phys.Rev.* **D79** (2009) 054507, [arXiv:0811.3640 \[hep-lat\]](#).
- [3] C. Bernard, C. E. DeTar, M. Di Pierro, A. El-Khadra, R. Evans, *et al.*, “The $\bar{B} \rightarrow D^* \ell \bar{\nu}$ form factor at zero recoil from three-flavor lattice QCD: A Model independent determination of $|V_{cb}|$,” *Phys.Rev.* **D79** (2009) 014506, [arXiv:0808.2519 \[hep-lat\]](#).
- [4] **BaBar** Collaboration, R. Kowalewski, “Status of $|V_{ub}|$ and $|V_{cb}|$ determinations,” *PoS FPCP2010* (2010) 028.
- [5] T. Mannel, “Determination of $|V_{ub}|$ and $|V_{cb}|$: A Theory Perspective,” *PoS FPCP2010* (2010) 029.
- [6] G. Ricciardi, “Status of $|V_{cb}|$ and $|V_{ub}|$ CKM matrix elements,” [arXiv:1412.4288 \[hep-ph\]](#).
- [7] C.-H. Chen and S.-h. Nam, “Left-right mixing on leptonic and semileptonic $b \rightarrow u$ decays,” *Phys.Lett.* **B666** (2008) 462–466, [arXiv:0807.0896 \[hep-ph\]](#).
- [8] A. Crivellin, “Effects of right-handed charged currents on the determinations of $|V_{ub}|$ and $|V_{cb}|$,” *Phys.Rev.* **D81** (2010) 031301, [arXiv:0907.2461 \[hep-ph\]](#).
- [9] A. J. Buras, K. Gemmler, and G. Isidori, “Quark flavour mixing with right-handed currents: an effective theory approach,” *Nucl.Phys.* **B843** (2011) 107–142, [arXiv:1007.1993 \[hep-ph\]](#).
- [10] A. Crivellin and S. Pokorski, “Can the differences in the determinations of V_{ub} and V_{cb} be explained by New Physics?,” *Phys.Rev.Lett.* **114** (2015) 011802, [arXiv:1407.1320 \[hep-ph\]](#).
- [11] **Fermilab Lattice, MILC** Collaboration, J. A. Bailey *et al.*, “ $|V_{ub}|$ from $B \rightarrow \pi \ell \nu$ decays and (2+1)-flavor lattice QCD,” [arXiv:1503.07839 \[hep-lat\]](#).
- [12] J. Flynn, T. Izubuchi, T. Kawanai, C. Lehner, A. Soni, *et al.*, “The $B \rightarrow \pi \ell \bar{\nu}$ and $B_s \rightarrow K \ell \bar{\nu}$ form factors and $|V_{ub}|$ from 2+1-flavor lattice QCD with domain-wall light quarks and relativistic heavy quarks,” [arXiv:1501.05373 \[hep-lat\]](#).
- [13] J. A. Bailey, A. Bazavov, C. Bernard, C. Bouchard, C. DeTar, *et al.*, “Update of $|V_{cb}|$ from the $\bar{B} \rightarrow D^* \ell \bar{\nu}$ form factor at zero recoil with three-flavor lattice QCD,” *Phys.Rev.* **D89** no. 11, (2014) 114504, [arXiv:1403.0635 \[hep-lat\]](#).
- [14] **BaBar** Collaboration, J. Lees *et al.*, “Evidence for an excess of $\bar{B} \rightarrow D^{(*)} \tau^- \bar{\nu}_\tau$ decays,” *Phys.Rev.Lett.* **109** (2012) 101802, [arXiv:1205.5442 \[hep-ex\]](#).
- [15] **LHCb RICH Group** Collaboration, M. Adinolfi *et al.*, “Performance of the LHCb RICH detector at the LHC,” *Eur.Phys.J.* **C73** (2013) 2431, [arXiv:1211.6759 \[physics.ins-det\]](#).
- [16] **LHCb** Collaboration, R. Aaij *et al.*, “Study of the kinematic dependences of Λ_b^0 production in pp collisions and a measurement of the $\Lambda_b^0 \rightarrow \Lambda_c^+ \pi^-$ branching fraction,” *JHEP* **1408** (2014) 143, [arXiv:1405.6842 \[hep-ex\]](#).
- [17] F. Cardarelli and S. Simula, “Isgur-Wise form-factors of heavy baryons within a light front constituent quark model,” *Phys.Lett.* **B421** (1998) 295–302, [arXiv:hep-ph/9711207 \[hep-ph\]](#).
- [18] H. G. Dosch, E. Ferreira, M. Nielsen, and R. Rosenfeld, “Evidence from QCD sum rules for large violation of heavy quark symmetry in Λ_b semileptonic decay,” *Phys.Lett.* **B431** (1998) 173–178, [arXiv:hep-ph/9712350 \[hep-ph\]](#).
- [19] C.-S. Huang, C.-F. Qiao, and H.-G. Yan, “Decay $\Lambda_b \rightarrow p \ell \bar{\nu}$ in QCD sum rules,” *Phys.Lett.* **B437** (1998) 403–407, [arXiv:hep-ph/9805452 \[hep-ph\]](#).
- [20] R. Marques de Carvalho, F. Navarra, M. Nielsen, E. Ferreira, and H. G. Dosch, “Form-factors and decay rates for heavy Λ semileptonic decays from QCD sum rules,” *Phys.Rev.* **D60** (1999) 034009, [arXiv:hep-ph/9903326 \[hep-ph\]](#).
- [21] M.-q. Huang and D.-W. Wang, “Light cone QCD sum rules for the semileptonic decay $\Lambda_b \rightarrow p \ell \bar{\nu}$,” *Phys.Rev.* **D69** (2004) 094003, [arXiv:hep-ph/0401094 \[hep-ph\]](#).
- [22] M. Pervin, W. Roberts, and S. Capstick, “Semileptonic decays of heavy Λ baryons in a quark model,” *Phys.Rev.* **C72** (2005) 035201, [arXiv:nucl-th/0503030 \[nucl-th\]](#).
- [23] H.-W. Ke, X.-Q. Li, and Z.-T. Wei, “Diquarks and $\Lambda_b \rightarrow \Lambda_c$ weak decays,” *Phys.Rev.* **D77** (2008) 014020, [arXiv:0710.1927 \[hep-ph\]](#).
- [24] Y.-M. Wang, Y.-L. Shen, and C.-D. Lu, “ $\Lambda_b \rightarrow p, \Lambda$ transition form factors from QCD light-cone sum rules,” *Phys.Rev.* **D80** (2009) 074012, [arXiv:0907.4008 \[hep-ph\]](#).
- [25] K. Azizi, M. Bayar, Y. Sarac, and H. Sundu, “Semileptonic $\Lambda_{b,c}$ to Nucleon Transitions in Full QCD at Light Cone,” *Phys.Rev.* **D80** (2009) 096007, [arXiv:0908.1758 \[hep-ph\]](#).
- [26] A. Khodjamirian, C. Klein, T. Mannel, and Y.-M. Wang, “Form Factors and Strong Couplings of Heavy Baryons from QCD Light-Cone Sum Rules,” *JHEP* **1109** (2011) 106, [arXiv:1108.2971 \[hep-ph\]](#).
- [27] T. Gutsche, M. A. Ivanov, J. G. Körner, V. E. Lyubovitskij, and P. Santorelli, “Heavy-to-light semileptonic decays of Λ_b and Λ_c baryons in the covariant confined quark model,” [arXiv:1410.6043 \[hep-ph\]](#).
- [28] T. Gutsche, M. A. Ivanov, J. G. Körner, V. E. Lyubovitskij, P. Santorelli, *et al.*, “The semileptonic decay $\Lambda_b \rightarrow \Lambda_c \tau^- \bar{\nu}_\tau$ in the covariant confined quark model,” [arXiv:1502.04864 \[hep-ph\]](#).
- [29] W. Detmold, C.-J. D. Lin, S. Meinel, and M. Wingate, “ $\Lambda_b \rightarrow p \ell^- \bar{\nu}_\ell$ form factors from lattice QCD with static b quarks,” *Phys.Rev.* **D88** (2013) 014512, [arXiv:1306.0446 \[hep-lat\]](#).
- [30] T. Mannel, W. Roberts, and Z. Ryzak, “Baryons in the heavy quark effective theory,” *Nucl.Phys.* **B355** (1991) 38–53.
- [31] F. Hussain, J. Körner, M. Kramer, and G. Thompson, “On heavy baryon decay form-factors,” *Z.Phys.* **C51** (1991) 321–328.
- [32] F. Hussain, D.-S. Liu, M. Kramer, J. Körner, and S. Tawfiq, “General analysis of weak decay form-factors in heavy to heavy and heavy to light baryon transitions,” *Nucl.Phys.* **B370** (1992) 259–277.

- [33] **UKQCD** Collaboration, K. Bowler *et al.*, “First lattice study of semileptonic decays of Λ_b and Ξ_b baryons,” *Phys.Rev.* **D57** (1998) 6948–6974, [arXiv:hep-lat/9709028 \[hep-lat\]](#).
- [34] S. A. Gottlieb and S. Tamhankar, “A Lattice study of Λ_b semileptonic decay,” *Nucl.Phys.Proc.Suppl.* **119** (2003) 644–646, [arXiv:hep-lat/0301022 \[hep-lat\]](#).
- [35] S. Meinel, “Flavor physics with Λ_b baryons,” PoS **LATTICE2013** (2014) 024, [arXiv:1401.2685 \[hep-lat\]](#).
- [36] **RBC, UKQCD** Collaboration, Y. Aoki *et al.*, “Continuum Limit Physics from 2+1 Flavor Domain Wall QCD,” *Phys.Rev.* **D83** (2011) 074508, [arXiv:1011.0892 \[hep-lat\]](#).
- [37] C. Bourrely, I. Caprini, and L. Lellouch, “Model-independent description of $B \rightarrow \pi \ell \nu$ decays and a determination of $|V_{ub}|$,” *Phys.Rev.* **D79** (2009) 013008, [arXiv:0807.2722 \[hep-ph\]](#).
- [38] T. Feldmann and M. W. Yip, “Form Factors for $\Lambda_b \rightarrow \Lambda$ Transitions in SCET,” *Phys.Rev.* **D85** (2012) 014035, [arXiv:1111.1844 \[hep-ph\]](#).
- [39] S. Weinberg, “Charge symmetry of weak interactions,” *Phys.Rev.* **112** (1958) 1375–1379.
- [40] S. Sasaki and T. Yamazaki, “Lattice study of flavor SU(3) breaking in hyperon beta decay,” *Phys.Rev.* **D79** (2009) 074508, [arXiv:0811.1406 \[hep-ph\]](#).
- [41] Y. Iwasaki, “Renormalization group analysis of lattice theories and improved lattice action. 2. Four-dimensional nonabelian $SU(N)$ gauge model,”.
- [42] Y. Iwasaki and T. Yoshie, “Renormalization group improved action for $SU(3)$ lattice gauge theory and the string tension,” *Phys.Lett.* **B143** (1984) 449.
- [43] D. B. Kaplan, “A Method for simulating chiral fermions on the lattice,” *Phys.Lett.* **B288** (1992) 342–347, [arXiv:hep-lat/9206013](#).
- [44] V. Furman and Y. Shamir, “Axial symmetries in lattice QCD with Kaplan fermions,” *Nucl.Phys.* **B439** (1995) 54–78, [arXiv:hep-lat/9405004](#).
- [45] Y. Shamir, “Chiral fermions from lattice boundaries,” *Nucl.Phys.* **B406** (1993) 90–106, [arXiv:hep-lat/9303005](#).
- [46] E. Eichten and B. R. Hill, “Renormalization of Heavy - Light Bilinears and f_B for Wilson Fermions,” *Phys.Lett.* **B240** (1990) 193.
- [47] A. X. El-Khadra, A. S. Kronfeld, and P. B. Mackenzie, “Massive fermions in lattice gauge theory,” *Phys.Rev.* **D55** (1997) 3933–3957, [arXiv:hep-lat/9604004 \[hep-lat\]](#).
- [48] S. Aoki, Y. Kuramashi, and S.-i. Tominaga, “Relativistic heavy quarks on the lattice,” *Prog.Theor.Phys.* **109** (2003) 383–413, [arXiv:hep-lat/0107009 \[hep-lat\]](#).
- [49] S. Aoki, Y. Kayaba, and Y. Kuramashi, “A Perturbative determination of mass dependent $O(a)$ improvement coefficients in a relativistic heavy quark action,” *Nucl.Phys.* **B697** (2004) 271–301, [arXiv:hep-lat/0309161 \[hep-lat\]](#).
- [50] H.-W. Lin and N. Christ, “Non-perturbatively Determined Relativistic Heavy Quark Action,” *Phys.Rev.* **D76** (2007) 074506, [arXiv:hep-lat/0608005 \[hep-lat\]](#).
- [51] **RBC, UKQCD** Collaboration, Y. Aoki *et al.*, “Nonperturbative tuning of an improved relativistic heavy-quark action with application to bottom spectroscopy,” *Phys.Rev.* **D86** (2012) 116003, [arXiv:1206.2554 \[hep-lat\]](#).
- [52] Z. S. Brown, W. Detmold, S. Meinel, and K. Orginos, “Charmed bottom baryon spectroscopy from lattice QCD,” *Phys.Rev.* **D90** (2014) 094507, [arXiv:1409.0497 \[hep-lat\]](#).
- [53] W. Detmold, C.-J. D. Lin, S. Meinel, and M. Wingate, “ $\Lambda_b \rightarrow \Lambda \ell^+ \ell^-$ form factors and differential branching fraction from lattice QCD,” *Phys. Rev. D* **87**, **074502** (2013) , [arXiv:1212.4827 \[hep-lat\]](#).
- [54] S. Meinel, “Bottomonium spectrum at order v^6 from domain-wall lattice QCD: Precise results for hyperfine splittings,” *Phys.Rev.* **D82** (2010) 114502, [arXiv:1007.3966 \[hep-lat\]](#).
- [55] S. Hashimoto, A. X. El-Khadra, A. S. Kronfeld, P. B. Mackenzie, S. M. Ryan, *et al.*, “Lattice QCD calculation of $\bar{B} \rightarrow D \ell \bar{\nu}$ decay form-factors at zero recoil,” *Phys.Rev.* **D61** (1999) 014502, [arXiv:hep-ph/9906376 \[hep-ph\]](#).
- [56] A. X. El-Khadra, A. S. Kronfeld, P. B. Mackenzie, S. M. Ryan, and J. N. Simone, “The Semileptonic decays $B \rightarrow \pi \ell \nu$ and $D \rightarrow \pi \ell \nu$ from lattice QCD,” *Phys.Rev.* **D64** (2001) 014502, [arXiv:hep-ph/0101023 \[hep-ph\]](#).
- [57] C. Lehner, “Automated lattice perturbation theory and relativistic heavy quarks in the Columbia formulation,” PoS **LATTICE2012** (2012) 126, [arXiv:1211.4013 \[hep-lat\]](#).
- [58] C. Lehner, “PhySyHCal.” <http://www.lhnr.de/physyhcal/>.
- [59] **Fermilab Lattice, MILC** Collaboration, J. A. Bailey *et al.*, “The $B \rightarrow D \ell \nu$ form factors at nonzero recoil and $|V_{cb}|$ from 2 + 1-flavor lattice QCD,” [arXiv:1503.07237 \[hep-lat\]](#).
- [60] N. H. Christ, J. M. Flynn, T. Izubuchi, T. Kawanai, C. Lehner, *et al.*, “B-meson decay constants from 2+1-flavor lattice QCD with domain-wall light quarks and relativistic heavy quarks,” [arXiv:1404.4670 \[hep-lat\]](#).
- [61] W. Detmold, C. D. Lin, and S. Meinel, “Calculation of the heavy-hadron axial couplings g_1 , g_2 , and g_3 using lattice QCD,” *Phys.Rev.* **D85** (2012) 114508, [arXiv:1203.3378 \[hep-lat\]](#).
- [62] C. Morningstar and M. J. Peardon, “Analytic smearing of $SU(3)$ link variables in lattice QCD,” *Phys.Rev.* **D69** (2004) 054501, [arXiv:hep-lat/0311018 \[hep-lat\]](#).
- [63] G. Colangelo, S. Durr, A. Juttner, L. Lellouch, H. Leutwyler, *et al.*, “Review of lattice results concerning low energy particle physics,” *Eur.Phys.J.* **C71** (2011) 1695, [arXiv:1011.4408 \[hep-lat\]](#).
- [64] S. R. Beane, “Nucleon masses and magnetic moments in a finite volume,” *Phys.Rev.* **D70** (2004) 034507, [arXiv:hep-lat/0403015 \[hep-lat\]](#).
- [65] S. R. Beane and M. J. Savage, “Baryon axial charge in a finite volume,” *Phys.Rev.* **D70** (2004) 074029, [arXiv:hep-ph/0404131 \[hep-ph\]](#).
- [66] W. Detmold, C.-J. D. Lin, and S. Meinel, “Axial couplings in heavy hadron chiral perturbation theory at the next-to-leading order,” *Phys.Rev.* **D84** (2011) 094502, [arXiv:1108.5594 \[hep-lat\]](#).

- [67] A. S. Kronfeld, “Application of heavy quark effective theory to lattice QCD. 1. Power corrections,” *Phys.Rev.* **D62** (2000) 014505, [arXiv:hep-lat/0002008](#) [[hep-lat](#)].
- [68] J. Harada, S. Hashimoto, K.-I. Ishikawa, A. S. Kronfeld, T. Onogi, *et al.*, “Application of heavy quark effective theory to lattice QCD. 2. Radiative corrections to heavy light currents,” *Phys.Rev.* **D65** (2002) 094513, [arXiv:hep-lat/0112044](#) [[hep-lat](#)].
- [69] J. Harada, S. Hashimoto, A. S. Kronfeld, and T. Onogi, “Application of heavy quark effective theory to lattice QCD. 3. Radiative corrections to heavy-heavy currents,” *Phys.Rev.* **D65** (2002) 094514, [arXiv:hep-lat/0112045](#) [[hep-lat](#)].
- [70] S. Shivashankara, W. Wu, and A. Datta, “ $\Lambda_b \rightarrow \Lambda_c \tau \bar{\nu}_\tau$ Decay in the Standard Model and with New Physics,” [arXiv:1502.07230](#) [[hep-ph](#)].
- [71] **SciDAC, LHPC, UKQCD** Collaboration, R. G. Edwards and B. Joo, “The Chroma software system for lattice QCD,” *Nucl.Phys.Proc.Suppl.* **140** (2005) 832, [arXiv:hep-lat/0409003](#) [[hep-lat](#)].
- [72] **LHCb** Collaboration, R. Aaij *et al.*, “Determination of the quark coupling strength $|V_{ub}|$ using baryonic decays,” [arXiv:1504.01568](#) [[hep-ex](#)].